SYSTEMS BIOLOGY

Human physiomimetic model integrating microphysiological systems of the gut, liver, and brain for studies of neurodegenerative diseases

Martin Trapecar[1], Emile Wogram[2], Devon Svoboda[2]*, Catherine Communal[1], Attya Omer[2],
Tenzin Lungjangwa[2], Pierre Sphabmixay[2,3], Jason Velazquez[1†], Kirsten Schneider[1],
Charles W. Wright[1], Samuel Mildrum[1,4,5], Austin Hendricks[1,4,5], Stuart Levine[1,4,5],
Julien Muffat[2‡], Meelim Jasmine Lee[1], Douglas A. Lauffenburger[1,6], David Trumper[3,6],
Rudolf Jaenisch[2,5*§], Linda G. Griffith[1,3,7*§]

Slow progress in the fight against neurodegenerative diseases (NDs) motivates an urgent need for highly controlled in vitro systems to investigate organ-organ– and organ-immune–specific interactions relevant for disease pathophysiology. Of particular interest is the gut/microbiome-liver-brain axis for parsing out how genetic and environmental factors contribute to NDs. We have developed a mesofluidic platform technology to study gut-liver-cerebral interactions in the context of Parkinson's disease (PD). It connects microphysiological systems (MPSs) of the primary human gut and liver with a human induced pluripotent stem cell–derived cerebral MPS in a systemically circulated common culture medium containing CD4$^+$ regulatory T and T helper 17 cells. We demonstrate this approach using a patient-derived cerebral MPS carrying the PD-causing A53T mutation, gaining two important findings: (i) that systemic interaction enhances features of in vivo–like behavior of cerebral MPSs, and (ii) that microbiome-associated short-chain fatty acids increase expression of pathology-associated pathways in PD.

INTRODUCTION

The gut-brain axis operates as a bidirectional communication system integrating the central nervous system (CNS) with endocrine, metabolic, and immune signaling pathways (1). As a vital participant in this system, the microbiome and its metabolic products, including short-chain fatty acids (SCFA), directly and indirectly affect the broader gut-immune-liver-brain axis. Accumulating data implicate dysregulation of the gut-brain axis in a variety of pathologies from inflammatory bowel disease to neurodegenerative diseases (NDs) (2, 3).

The causality of multifactorial diseases involving the gut-brain axis are difficult to parse in animal models, as the highly convoluted nature of the systemic interactions are combined with interspecies differences in metabolism and immunology. For example, SCFA produced by fermentation in the human proximal colon (up to 600 mmol/day) can influence gut-brain communication and function directly or indirectly through immune, endocrine, vagal, and other humoral pathways (3). Microbial bioactives can affect the axis via local interactions with enteric nerves transduced to the CNS (vagal pathway) or, separately, via systemic circulation to organs and tissues (humoral pathway) and immune cells (immune pathway). The liver is prominently involved in the humoral and immune pathways as the first draining point of the large intestine. In animal models, those individual routes of action and connections to pathology are difficult to deconvolute. Furthermore, the influence of individual microbiome-derived metabolites cannot be readily separated from the context of the entire gut milieu. This drives a need for causality-focused, human-based, preclinical models that incorporate engineering conceptualization of diseases such as new platform technologies designed to capture the crucial yet complex physiological phenomena in vitro in a systematic and scalable manner.

Parkinson's disease (PD) is prototypical of NDs, with links to the gut microbiome and systemic immune function, for which etiologies and effective therapies remain poorly defined. PD is a late age-onset, chronic, neurodegenerative disorder characterized by inflammation, accumulation of Lewy bodies in neurons, and cell death. Approximately 90% of PD cases are sporadic (4). However, familial PD has been linked to dominant mutations, such as the A53T mutation, causing misfolding and aggregation of α-synuclein (αSyn) with formation of Lewy bodies (5). Neurons throughout the nervous system are affected, causing especially pronounced damage to dopaminergic neurons in the brain and associated symptomatic loss of motor control. Environmental and genetic factors have been associated with development of PD and other NDs.

A potentially important signaling link between the gut microbiome and the brain in the context of PD involves SCFA. A previous study with gnotobiotic mice implicated the presence of SCFA to faster progression toward PD in a mouse model of the disease (1). Intriguingly, recent data in mice also implicate the microbiome in increased inflammation related to amyotrophic lateral sclerosis—a phenomenon that is reduced in mice treated with broad-spectrum antibiotics (6). SCFA exert pleiotropic effects that may contribute to a brain phenotype: They are linked to the development of microglia, provide an important energy source for the brain, and influence neuronal

function (2). Moreover, SCFA modulate several major metabolic pathways in the liver that alter blood lipids and sugars and influence the inflammatory phenotypes of immune cells in the intestine, liver, and circulation (7, 8), thus indirectly influencing the microenvironment of the nervous system in ways that might potentiate or protect from development of PD or other NDs in humans.

Experiments performed in gnotobiotic mice cannot be translated directly into a protocol for experimentation on human patients. We therefore designed an in vitro all-human physiomimetic model that captures salient features observed in those studies as a demonstration for how continuously interlinked microphysiological systems (MPSs) can bring insights into human disease pathophysiology. MPSs are in vitro models that, under perfusion, mimic facets of physiological organ behavior (9). The goal of physiomimetic models is to define the essential elements of complex disease states involving multiple organ systems and capture these in the simplest possible MPS experimental configuration that will reveal useful insights. Here, we first define the physiomimetic model for parsing causality in the interconnection between the microbiome and early stages of NDs according to the following phenomena: (i) humoral and immune pathways connecting microbial metabolites (but not microbes) to the gut-liver-brain axis independently of endocrine and vagal pathways; (ii) how interaction between MPSs of the gut, liver, and circulating CD4$^+$ T cells affects maturation of neurons, astrocytes, and microglia; (iii) the effects of bioaccessible SCFA on cerebral MPSs that represent certain features of familial PD and those of healthy controls; and (iv) how increase or reduction of inflammatory mediators via SCFA and inclusion of CD4$^+$ T cells affects the PD phenotype.

On the basis of this conceptualization of the disease, we designed an experimental platform linking three complex MPSs—gut/immune, liver/immune, cerebral/immune—via a common culture media containing circulating immune cells in continuous coculture. The platform design simultaneously addresses several challenges required to accomplish the desired physiological integration, including (i) open system accommodating standard culture models for each MPS (e.g., Transwell insert for mucosal barrier), thus facilitating access to individual compartments for fluid sampling and comparison with literature for behaviors of individual MPSs; (ii) continuous recirculation of medium within each MPS to facilitate molecular and cellular transport between tissues and circulating medium with flow rates tailored to the needs of each individual MPS; (iii) continuous recirculation of a relatively small volume of common culture medium (5 ml) between MPSs at flow rates sufficient to exchange the entire culture volume over five times per day, with flow patterns that provide physiologically scaled ratios of systemic (25%) and portal (75%) circulation to the liver MPS; (iv) in addition to continuous flow between MPSs, independent fluid mixing within each MPS to enhance local molecular and cellular transport; (v) continuous recirculation of functionally viable immune cells; (vi) minimal loss of lipophilic medium components to platform adsorption; and (vii) moderate throughput on each platform, with three complete independent circuits per platform. While individual constraints have been addressed in other platforms, this is the first demonstration of integration of all components. The crucial elements of the approach include (i) unique on-board microfluidic pumps that are safe for immune cells and can be multiplexed on the platform, with individually addressable flow rates, to eliminate external tubing and minimize circulating medium volumes; (ii) elimination of polydimethylsiloxane (PDMS) by machining the platform from polycarbonate and using a non-PDMS elastomer on the pumps; and (iii) inclusion of gravity flow connections as part of the fluidic circuit, to offset any slight differences in pump flow rates arising from minor fabrication variances and thus control fluid volumes in individual compartments while minimizing the overall platform footprint (see details in Materials and Methods and Results). We take advantage of this on-board, platform-integrated pumping technology to conduct a proof-of-principle experiment demonstrating its potential utility for coculture with circulating immune cells, thus illuminating facets of complex systemic immune system–mediated processes.

Our findings using this physiomimetic model of early-onset PD indicate that the interaction of healthy cerebral MPS controls with MPSs of the gut-liver axis in the presence of circulating CD4 regulatory T cells (T$_{regs}$) and T helper 17 (T$_H$17) cells beneficially affects the cerebral MPS's phenotype. This includes increased expression of genes associated with maturity of neurons, astrocytes, and especially microglia. We observed pathology-related effects of systemic SCFA unique to MPSs of PD, but not in healthy controls. Hence, engineered human physiomimetic models can aid in our understanding of multifactorial NDs and complement in vivo animal models as tools to investigate disease causality.

RESULTS

Conceptualization of key biological phenomena informing experimental platform design

At a coarse-grain view, we considered the following biological phenomena in the conceptualization of a physiomimetic model of the gut-liver-brain axis (Fig. 1A and fig. S1A): (i) SCFA adsorption through a colon mucosal barrier incorporating innate immune cells, where the SCFA may be partially metabolized to influence production of soluble signaling molecules; (ii) transport through the portal circulation to the liver, where additional metabolism occurs by hepatocytes, and where the SCFA exert influence on innate immune Kupffer cells in the liver; and (iii) transport of soluble metabolites and inflammatory mediators through the systemic circulation to the brain along with (iv) migration of adaptive immune CD4$^+$ T cells via systemic circulation between the gut, liver, and the brain.

As MPSs represent relatively reductionist models of complex organ systems, we structured individual MPSs to reflect the above-described physiological features and scaled the relative cell numbers according to their physiological functions (Fig. 1A). The gut serves many functions, of which nutrient absorption and regulation of immune tolerance toward the commensal microbiome are among the most important. Cell lines that are often used to model some features of the colon barrier, such as the cancer-derived Caco-2 line, are not appropriate for modeling SCFA effects because of the stark differences in their metabolism and signaling compared to human primary tissues (10). We thus designed the gut MPS based on primary colon epithelial cells that were propagated as organoids and seeded as single cells on 12-well Transwells. Myeloid cells, like macrophages and dendritic cells, are both the first line of defense against pathogens in the gut and crucial modulators of epithelial homeostasis and tissue repair; hence, their integration into MPSs of the gut is an essential biological feature (11). We seeded peripheral blood mononuclear cell (PBMC)–derived macrophages and dendritic cells on the basolateral side of the Transwells harboring a differentiated primary epithelial monolayer (fig. S1B).

The liver receives most of its blood from the gut and plays a pivotal role in the metabolism of and immunity against gut-derived products.
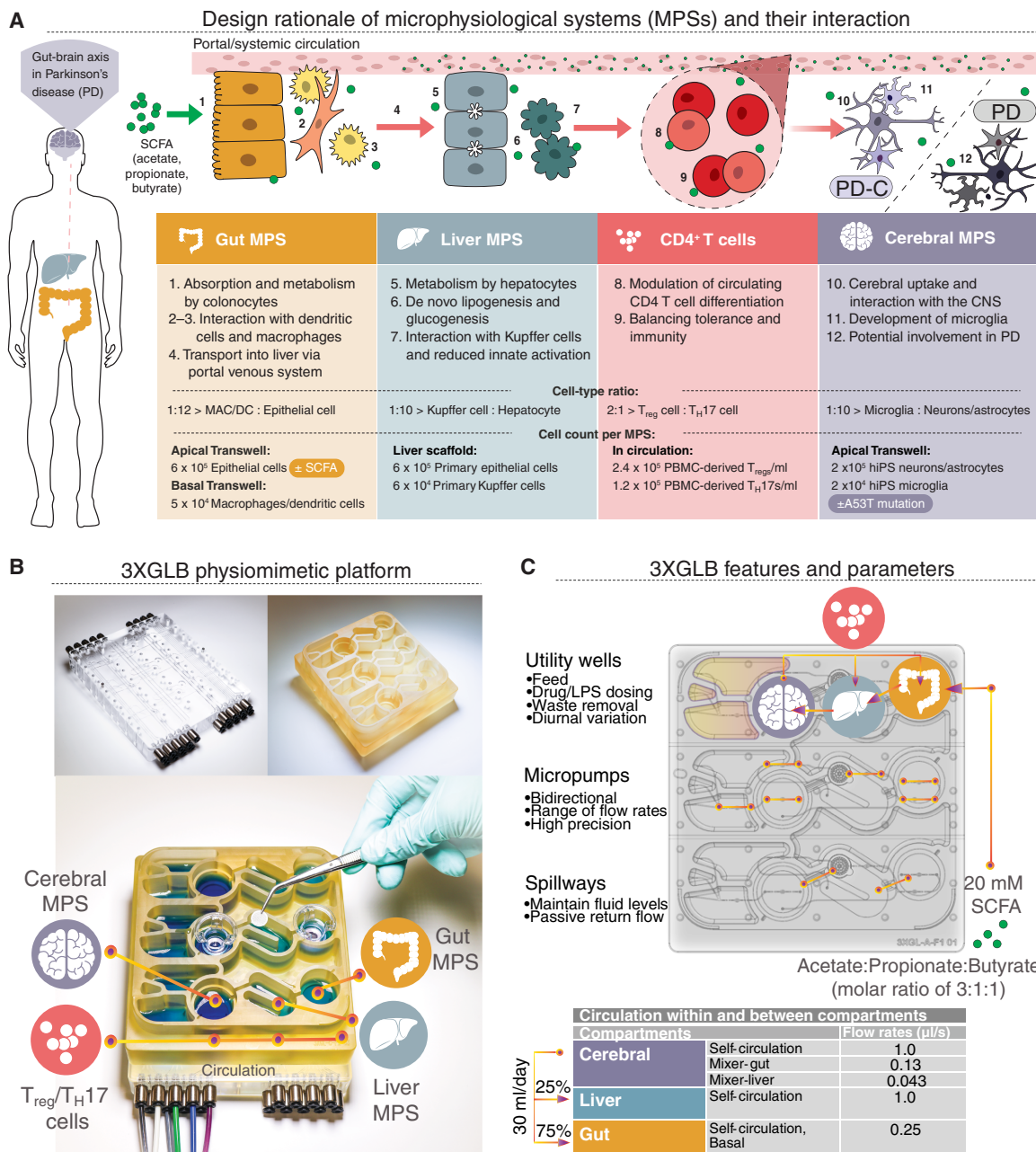
Fig. 1. Human 3XGLB physiomimetic system of the gut-liver-brain axis. (**A**) Schematic representation of the design rationale for the experimental approach and description of individual MPSs included in this study. (**B**) Top left: pneumatic plates machined in acrylic; top right: mesofluidic plate machined from monolithic polysulfone; bottom: 3X Gut-Liver-Brain (3XGLB) platform composed of pneumatic and fluidic plates with elastomeric polyurethane membrane in between them to form a pumping manifold with integrated fluid channels. The platform allows three-way interaction in three replicates where the center liver-specific MPS can be fluidically linked to two additional Transwell-based MPSs. Photo credit: Martin Trapecar, MIT. (**C**) Top view of the 3XGLB with identified fluidic and pumping properties as well as operational parameters (for more details, see fig. S1A).

The liver MPS was designed to capture the metabolic transformation of SCFA as well as features of the immunological environment. The microtissue comprised a coculture of human primary cryopreserved hepatocytes and Kupffer cells at physiological 10:1 ratio maintained in a culture medium permissive for retention of inflammation responses (*12*, *13*). Although it is technically feasible to include additional primary nonparenchymal cells (*14*), or cell lines representing

them (*15*), immune-metabolic cross-talk can be adequately represented in long-term culture by primary hepatocytes and Kupffer cells (*12*). Cells were seeded on a microperfused liver scaffold that allows for optimal oxygenation and nutrient flow (fig. S1C) (*12*).

Key players in perpetuating inflammation-related cerebral PD pathology are neurons, astrocytes, and microglia. We therefore adapted a well-established, robust model comprising human PD patient-derived

induced pluripotent stem cells (iPSCs) differentiated into neurons, astrocytes, and microglia cultured in a Transwell format amenable to incorporation on a mesofluidic platform (16). We used a neural differentiation method that gives rise to various types of CNS cells, as PD-associated pathology is not limited to the substantia nigra and dopaminergic neurons, but rather affects a wide variety of CNS cell types (17). The cerebral cell types used in this study were derived from human iPSCs (hiPSCs) that carry either the A53T mutation in αSyn (PD) or hiPSC corrected (PD-C) to wild-type healthy status (5), to enable isogenic comparison of disease and healthy cerebral tissue.

Microbiome-derived metabolites and their derivatives have been shown to affect the differentiation and function of T lymphocytes, most notably the balance between $CD4^+$ T_{regs} and T_H17 cells (8), both of which are implicated in PD. These two immune cell types play an important role in maintaining the balance between auto-immunity and immune tolerance where T_{regs} dampen inflammation by producing transforming growth factor–β (TGF-β) on one side and T_H17 cells (T_H17s) support inflammation by releasing the cytokines interleukin-17 (IL-17) and IL-22 (18) on the other. An increased number of T_H17 cells versus the frequency of T_{regs} in circulation has been observed in patients with PD, yet the exact contribution of this phenomenon is yet to be defined (19, 20). Moreover, in advanced stages of PD, T_H17 cells have been shown to be the first effector T cells to cross the disrupted blood-brain barrier (BBB). In this current study, we therefore integrated circulating PBMC-derived T_{reg} and T_H17 cells as a feature of the adaptive immune system that has been implicated in the progression of PD.

Capturing the biological phenomena described above in an in vitro experimental setting requires a platform technology that enables (i) continuous fluidic communication between MPSs as well as controllable circulation within each compartment, (ii) undisrupted continuous circulation of $CD4^+$ immune cells, and (iii) the incorporation of well-defined and validated cell culturing systems such as Transwell inserts that are routinely used by many medical researchers and (iv) that are engineered on a mesofluidic scale that allows for the interrogation of bigger media volumes and tissue mass as those offered by microfluidic setups.

The resulting 3XGLB (3X Gut-Liver-Brain) human physiomimetic system of the gut-liver-brain axis allows for the selective integration of key physiological features and MPSs (Fig. 1B and movie S1). The physiomimetic 3XGLB system was engineered to house three sets of three fluidically interconnected MPSs with adjustable, pneumatic intra- and intercompartmental circulation (Fig. 1C). The system features low-volume pumps that can circulate culture medium containing adaptive immune cells between the individual compartments, preserving immune cell viability (fig. S1D). Cell ratios and numbers of all MPSs were kept constant across all interaction studies (scaled as described in Fig. 1A) and are described in detail in Materials and Methods.

Physiomimetic interaction improves markers of cerebral MPS phenotype and maturity of neurons, astrocytes, and microglia

First, we aimed to understand how the physiomimetic interaction of cerebral MPSs with the gut and liver MPSs, as well as T_{reg}/T_H17 cells, affects expression of genes specific to the maturation and function of neurons, astrocytes, and microglia. We evaluated differential gene expression (DGE), enriched pathways in PD-C MPS tissue, and cytokine/chemokine concentrations in the shared common medium

(CM) during different modes of a 4-day interaction (Fig. 2A). Canonical functional tissue phenotypic markers, gut barrier integrity, and liver albumin production were preserved throughout tissue interaction (fig. S1, B and C). These functions were also maintained during interactions involving the PD MPSs and SCFA described below.

Interaction of the control PD-C cerebral MPSs with the gut and liver MPSs in the absence or presence of T_{reg}/T_H17 cells markedly affected its biology (Fig. 2B). DGE analysis of neuron-related genes (21, 22) (in collectively harvested neurons, astrocytes, and microglia) showed increased expression of genes important for homeostasis of mature neurons such as GAP43 and CNR1 and reduced expression of genes associated with neuronal progenitors (PAX6 and NCAM1) during gut-liver-cerebral interaction versus PD-C MPSs in isolation. This enhancement of neuronal maturation during interaction was more pronounced in the presence of T_{reg}/T_H17 cells (Fig. 2B). A similar trend was observed when analyzing astrocyte-related genes (23, 24), which showed increased expression of homeostatic genes and reduced expression of genes associated with astrocyte activation. However, the greatest and most significant fold changes in DGE were observed in those associated with maturation and immune activation of microglia (25, 26). In vivo–like maturation of microglia is particularly hard to achieve with current in vitro methods (26). Our data showed that the interaction of PD-C with gut and liver MPSs significantly favors expression of genes related to maturation of microglia such as CD14, MAFB, SPI1, and that of genes associated with microglia immune function among which are CD74, C3, and Human Leukocyte Antigen–DR isotype (HLA-DR)—especially in the presence of T_{reg}/T_H17 cells (Fig. 2B). Responsiveness of microglia to external stimuli via innate immune activation, major histocompatibility complex class II signaling, and activation of complement cascades is relevant for in vitro modeling of NDs.

Furthermore, transcriptional changes analyzed by PANTHER pathway enrichment (Fig. 2C) showed that interaction of the PD-C cerebral MPS with the liver and gut MPSs enhanced several pathways compared to isolated cerebral MPSs. These include integrin signaling, increased glycolysis, and axon guidance that are required for neuronal axonal growth and the establishment of neuronal connections (27). Moreover, dopamine and metabotropic glutamate receptor pathways important for neurotransmitter signaling were increased during the interaction (28). Addition of T_{reg}/T_H17 cells to the interacting MPSs further increased PD-C MPS expression of genes related to glycolysis and axonal guidance (Fig. 2D). Pathways related to cholesterol biosynthesis, serotonin receptor 5HT4, and oxytocin receptor–mediated signaling were increased in the presence of T_{reg}/T_H17 cells. Cholesterol in the brain is regulated independently of that in circulation and represents up to 25% of total body cholesterol, being largely produced by astrocytes and vital for electrical signal transmission as well as serotonin and oxytocin receptor signaling (29). Dysregulation of cholesterol synthesis in the brain is associated with a variety of NDs; thus, in vitro models of NDs capturing alterations in cholesterol metabolism are highly relevant for preclinical research.

Next, we characterized phenotypic markers and cytokines in circulating media during interactions and compared them to known clinical values (Fig. 2, E and F, and tables S1 and S2) as inflammatory status is an important benchmark for comparison of the microenvironment in vitro to that in vivo. Moreover, the starting media volumes and numbers/ratios of individual cell types across interaction replicates were kept constant in the engineered 3XGLB system, and a comparison to known in vivo clinical values offered important
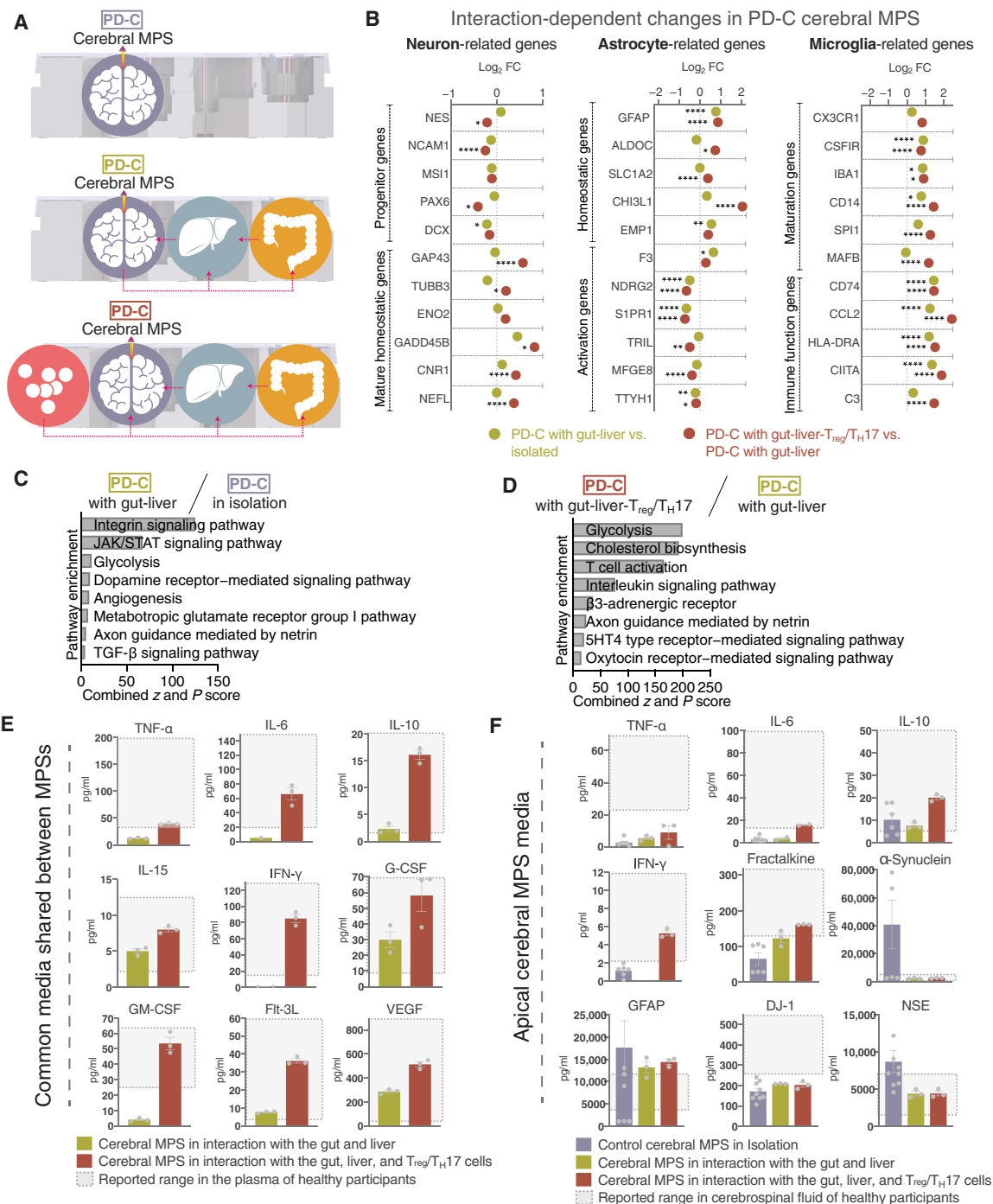
Fig. 2. Physiomimetic interaction increases in vivo markers of cerebral MPSs. (**A**) Schematic presentation of conditions compared in Fig. 1 (B to F) and tables S1 and S2. Top: Control PD-C cerebral MPS in isolation; middle: Control PD-C cerebral MPS in interaction with the gut and liver MPSs; bottom: Control PD-C MPS in interaction with the gut and liver MPSs and T_{reg}/T_H17 cells. (**B** to **D**) We jointly harvested neurons, astrocytes, and microglia of three separate replicates of control PD-C cerebral MPSs after a 4-day interaction with the gut and liver MPSs in the absence or presence of T_{reg}/T_H17 cells. (B) We compared DGE of neuron-, astrocyte-, and microglia-related genes between cerebral MPSs in isolation versus those in interaction. Significance is expressed as *$P < 0.05$, **$P < 0.001$, ****$P < 0.00001$. (C and D) PANTHER pathway enrichments in cerebral PD-C MPSs in interaction over those in isolation. Data represent averages of three replicates. Pathways are ranked on the basis of a combined z and P value score. (**E**) Concentrations of cytokines measured in the CM shared between MPSs after 96 hours of gut-liver-cerebral (PD-C) interaction studies with or without circulating T_{reg}/T_H17 cells and indicated reported values of the same proteins in human plasma (for exact values and references, see table S1). (**F**) Concentrations of cytokines and neuronal markers measured in the apical control PD-C MPS media after 96 hours in isolation or during the gut-liver-brain interaction studies with or without circulating T_{reg}/T_H17 cells and indicated reported values of the same proteins in human cerebrospinal fluid (for exact values and references, see table S2). Data represent averages of two to nine replicates after 4 days in culture. Error bars represent SEM. TNF-α, tumor necrosis factor–α; GFAP, glial fibrillary acidic protein.

guiding insight for ex vivo scaling of devices mimicking human physiology. Most of the cytokines and chemokines detected in the CM shared between the MPSs, especially in the presence of circulating T_{reg}/T_H17 cells, showed an overlap in concentration values with ranges reported for human plasma (Fig. 2E and table S1), where measured values reflect maximum concentrations accumulated at day 4 of culture in medium exchanged after 2 days of interaction. Similarly, we compared cytokine and neuronal marker concentrations in the apical compartment of the PD-C cerebral MPSs after 4 days in isolation or interaction (without interim media changes) with concentrations reported in the cerebrospinal fluid (CSF) of healthy human individuals (Fig. 2F and table S2). CSF cytokine concentrations are a reasonable proxy for brain interstitial cytokine values (30). Interaction of the cerebral MPSs with the gut and liver MPSs, especially in the presence of circulating T_{reg}/T_H17 cells, led to PD-C cytokine and neuronal marker concentrations to be closer to ranges reported in CSF of healthy adults. This is particularly true for the release of αSyn, which occupies the center stage in PD research (Fig. 2F). In the presence of T_{reg}/T_H17 cells, levels of the cytokines granulocyte-macrophage colony-stimulating factor (GM-CSF), fractalkine, and interferon-γ were insignificantly increased in both the common and apical cerebral medium, which might explain the increased expression of genes related to maturation of microglia that underpins the importance of immune-tissue interactions in achieving a greater in vivo–like phenotype.

Analysis of both transcriptomic and multiplexed cytokine/neuronal marker data indicates several functional parameters of control PD-C MPSs to be increased when in interaction with the gut, liver, and $CD4^+$ T cells as opposed to its expression in isolation, suggesting better alignment with in vivo function.

PD cerebral MPSs exhibit disease-specific transcriptomic, inflammatory, and metabolomic characteristics in isolation

Patient-specific hiPSCs are valuable in studying diseases where genetic background variation poses a significant effect, as they enable experiments under genetically well-defined conditions (5). Here, we used hiPSC-derived neurons, astrocytes, and microglia carrying the PD-associated A53T mutation to establish the PD cerebral MPS. We also used same-donor hiPSC-derived neurons, astrocytes, and microglia with the corrected mutation for the control PD-C MPS.

We first examined behaviors of PD versus PD-C MPSs in isolation. Neurons of the cerebral MPSs used in this study exhibit expression of neuron-specific markers and release neuron-specific proteins. Ramified microglia, astrocytes, and neurons that formed a multilayered three-dimensional (3D) structure when grown on microporous membranes exhibited comparable morphological features in the PD and PD-C MPSs (Fig. 3A). However, a global untargeted metabolomic screen of the cell culture media of both MPSs after 4 days of culture revealed a stark contrast between their metabolic functions. The most enriched metabolic pathways in the PD MPSs, as compared to PD-C, were the mevalonate metabolism and creatine metabolism (Fig. 3B). We were able to predict the phenotype of the MPS based solely on the metabolite profiles analyzed using a Random Forest algorithm (fig. S2A).

Comparison of DGE between mutant and control MPSs revealed significant transcriptional differences. In particular, the PD cerebral MPS showed increased expression of CYP26B1, an enzyme-inactivating retinoic acid as a tissue-patterning mechanism governing development of the hindbrain (31). GPNMB, a glycoprotein shown to be elevated concurrently with glycophospholipids in the substantia nigra region of patients with PD (32), was overexpressed as well (Fig. 3C). On the basis of WikiPathways, pathways of microglial activation and cytoplasmic ribosomal proteins were more highly expressed in the PD MPS. Conversely, pathways associated with nitric oxide–mediated neuroprotection and the Parkin-ubiquitin proteasomal system pathway, which is critical for proper regulation of protein turnover (33), are more enriched in the PD-C control MPSs (Fig. 3D).

Multiplex cytokine analysis at day 4 of culture of the individual PD and PD-C MPSs showed subtle differences between the two conditions where PD MPSs appear to release a slightly higher amount of inflammatory cytokines tumor necrosis factor–α (TNF-α), IL-6, and IL-17A but significantly less of the chemokines fractalkine, an important signaling molecule between neurons and microglia and regulator of microglia activation (34), and monocyte chemoattractant protein (MCP)–1 and MCP-3 (fig. S2B). The neuron-specific protein neuron-specific enolase (NSE) and the astrocyte-derived protein glial fibrillary acidic protein (GFAP) are produced by the MPSs at similar rates; however, the PD MPSs release significantly less DJ-1, also known as PD protein 7, that inhibits aggregation of αSyn (35). This is consistent with PD MPSs releasing less soluble, multiplex-detectable αSyn and in agreement with clinical observations (Fig. 3E) (36).

When transcriptomic changes were probed for disease-associated patterns via the GEO Diseases database, genes associated with neurodegenerative malfunction and PD were found to be enriched in the PD MPSs—in particular, genes related to ribosomal proteins (Fig. 3F).

While PD in a clinical setting is most commonly associated with αSyn protein misfolding and aggregation in dopaminergic neurons in the substantia nigra region of the brain, other neuronal cell types like enteric neurons and regions of the CNS are also affected by synucleinopathy in PD (37). Our data indicate that even under fairly reductionist conditions, PD cerebral MPSs carrying the A53T mutation exhibit fundamental metabolic and transcriptional differences reminiscent of PD when compared to the control PD-C cerebral MPSs.

SCFA universally decrease inflammatory cytokines and alter secretion of neuronal biomarkers during physiomimetic interaction with and without circulating T_{reg}/T_H17 cells

After evaluating the steady-state influence of physiomimetic interaction of the PD-C MPS with gut and liver MPSs as well as T_{reg}/T_H17 cells and characterization of the PD MPS, we proceeded with interaction studies elucidating the effect of gut MPS-derived SCFA on the phenotype of PD versus PD-C cerebral MPSs. Using the 3XGLB platform, we fluidically connected the gut, liver, and cerebral MPSs in the absence or presence of circulating T_{reg}/T_H17 cells, included in a ratio of 2:1 (Fig. 4A). We added 20 mM of total SCFA in a physiological molar ratio between acetate, propionate, and butyrate (6:2:2) into the apical compartment of the gut MPSs and proceeded with a 4-day interaction experiment. In a gut-liver interaction study without a cerebral MPS, SCFA have been shown to be readily absorbed by the gut MPS (ulcerative colitis donor), where 50% of butyrate was consumed by the epithelium and the remaining SCFA, mainly propionate and butyrate, were metabolized by the healthy liver MPS, which led to increased de novo lipogenesis and glycolysis (8). Acetate remained the most abundant SCFA in systemic circulation that resembles known in vivo distribution and metabolic dynamics of SCFA (38).
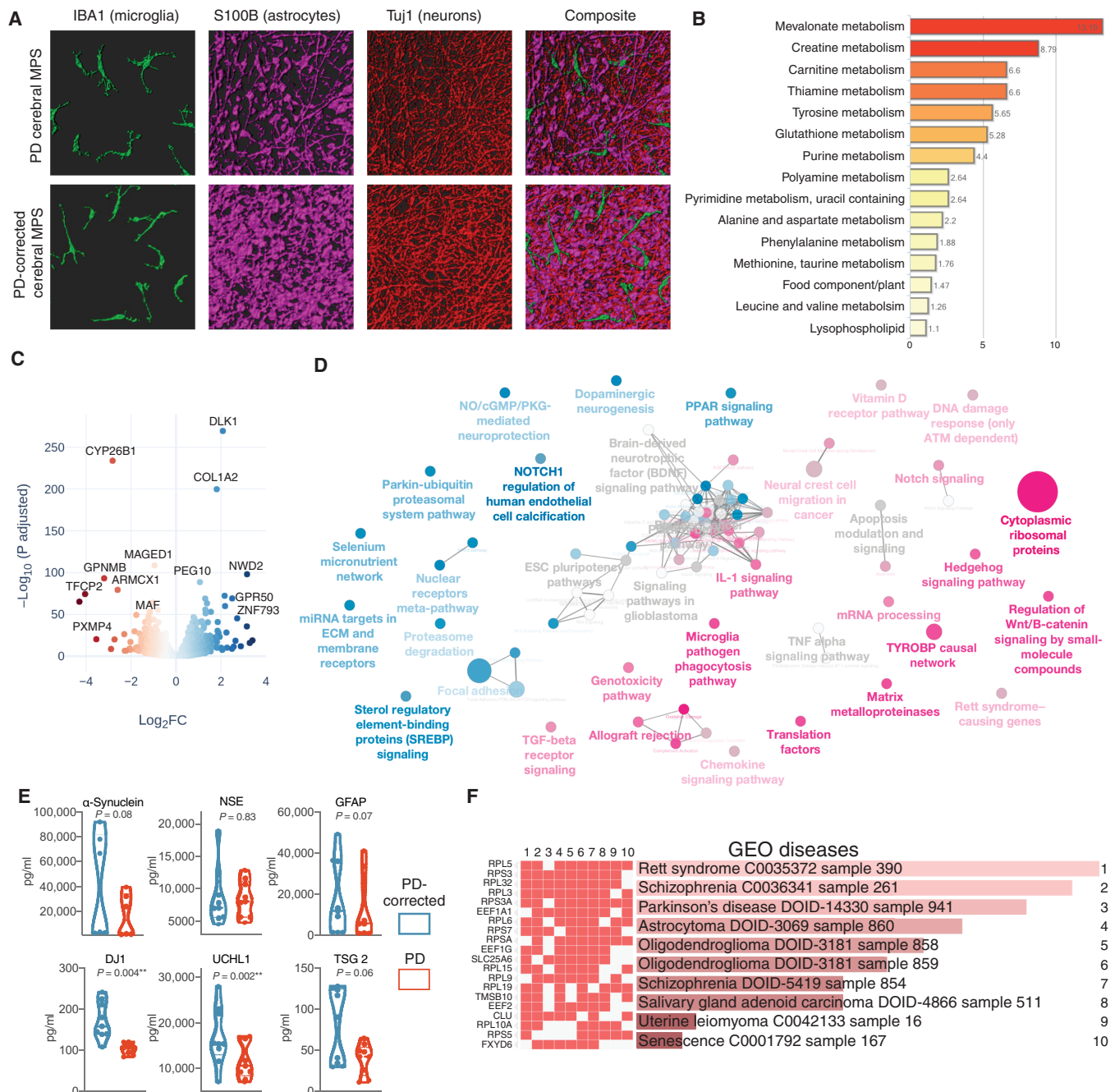
Fig. 3. PD cerebral MPSs exhibit PD-associated transcriptional and metabolic features. (**A**) Representative, 3D rendered confocal images of the PD (top) and control PD-C (bottom) cerebral MPSs composed of hiPSC-derived microglia (green), astrocytes (purple), and neurons (red) cocultured on 0.4-μm microporous 24-well Transwells. (**B**) Metabolic pathway enrichment in apical cerebral media after 4 days of culture of the PD cerebral MPSs when compared to the PD-C control MPS. (**C**) Volcano plot of DGE among neurons, astrocytes, and microglia in PD MPSs (red) over PD-C control MPSs (blue). (**D**) ClueGO Network of enriched (magenta) and suppressed (blue) WikiPathway pathways in PD cerebral MPSs based on DGE shown under (C). (**E**) Concentration (ng/ml) of multiplexed neuronal markers in apical media of the PD and PD-C MPSs after 4 days of culture in isolation. Data represent six to nine biological replicates from two to three independent experiments. Significance was determined with paired *t* test. Lines in violin plots denote distribution quartiles. (**F**) DGE pathway enrichments in PD cerebral MPSs as compared to control PD-C MPSs based on the GEO Diseases database. Diseases are ranked by combined *P* value and rank score. (B to D and F) Data represent averages of three replicates after 4 days in coculture.

We first evaluated the potential of SCFA to alter the inflammatory environment of the CM shared between the MPSs and the apical compartment of the cerebral MPSs as well as the apical release of neurological biomarkers during interaction. We constructed an unsupervised principal components analysis (PCA) model from

39 cytokine/chemokine analytes measured in the basal CM and apical cerebral MPS compartments during all interactions, with and without T_{reg}/T_H17 cells (Fig. 4B). Clear separation along the diagonal was observed on the basis of whether the sample origin was basal or apical media and the absence or presence of T_{reg}/T_H17 cells (round
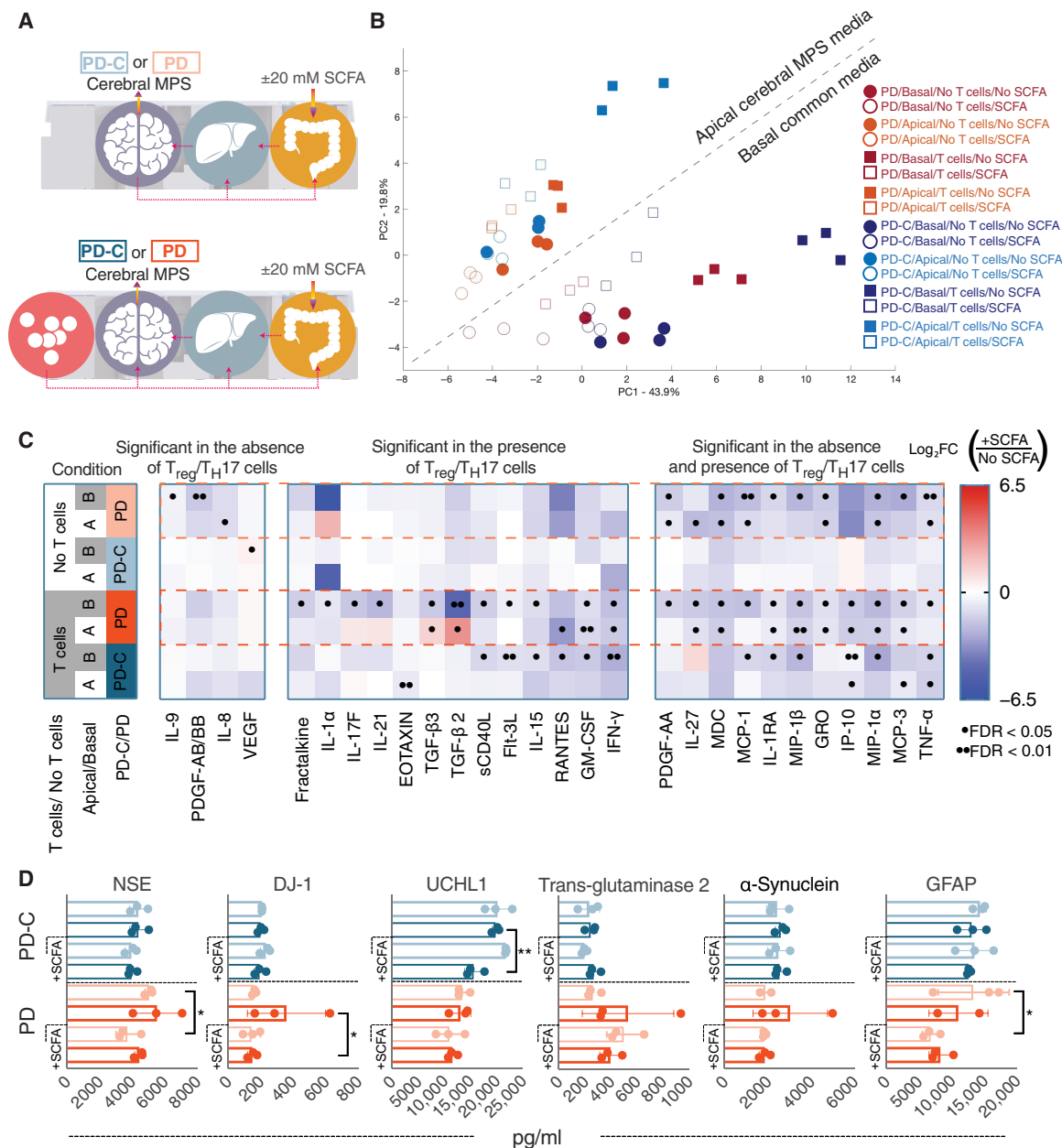
Fig. 4. SCFA universally reduce inflammatory cytokines during physiomimetic interaction. (**A**) Schematic presentation of conditions compared in Fig. 1 (B to D). (**B**) PCA of all multiplexed cytokines/chemokines after 4 days of interactions in the CM shared between the MPSs and apical cerebral MPS media. Samples primarily separate from top to bottom depending on the sampling site as indicated by the dotted line and from left to right depending on the presence of SCFA (empty markers) versus absence of SCFA (filled markers). Samples were z scored before PCA. (**C**) Presence of SCFA significantly reduces concentrations of most analytes regardless of PD or PD-C genotype, as illustrated in a heatmap showing log2 fold changes (log2FC) in cytokine, chemokine, and growth factor concentrations between SCFA-treated and untreated groups (see leftmost column). The log2FC values are annotated for significance based on the false discovery rate (FDR) where •FDR < 0.05, ••FDR < 0.01. Heatmaps comparing actual concentrations can be found in fig. S3. (**D**) Concentration (ng/ml) of multiplexed neuronal markers in apical media of the interacting cerebral MPSs after 4 days of culture. Significance was determined with a paired t test where *P < 0.05, **P < 0.001. Each interacting condition had three replicates, and the results present their averages.

or square sample labeling). The difference in cytokine ratios in the CM to the apical cerebral MPS media indicates that passive transport of signaling molecules into the apical compartment is insignificant, despite the lack of an endothelial BBB. Hence, a brain-specific environment was maintained during interaction.

Notably, when focusing on a specific media compartment (apical or basal) and presence of $T_{reg}/T_{H}17$ cells, samples separated on the

basis of ±SCFA treatment (i.e., empty versus filled markers) but not PD and PD-C genotype; empty markers (+SCFA) are left-shifted on the PC1 axis compared to their filled (no SCFA) counterparts. $T_{H}17$ cells are one of the first types of lymphocytes to cross the BBB under inflammatory conditions, and their production of IL-17 contributes to PD progression, while, at the same time, a reduced ratio of T_{regs} to $T_{H}17$ cells in blood of patients with PD has been observed (19, 20).

SCFA have previously been reported to promote T_{reg} differentiation as well as to increase T cell effector function (*39*).

To further illuminate the influences of SCFA captured in the left-shift of the +SCFA compared to −SCFA paired conditions along the PC1 axis in the PCA, we generated a heatmap of log_2 fold changes in cytokine, chemokine, and growth factor concentration values between SCFA-treated and untreated groups for each condition (Fig. 4C). A two-sided *t* test was conducted to compare the sample values +SCFA and −SCFA within a given condition, and values are annotated for significance on the heatmap based on the false discovery rate. The heatmap is organized to group together (i) analytes that are significant only for groups in the absence of T_{reg}/T_H17 cells, (ii) analytes that are significant only for groups with T_{reg}/T_H17 cells, and (iii) analytes that are significant across all conditions. The overwhelming majority of analytes are significantly suppressed by the presence of SCFA during interaction, regardless of the PD genotype and regardless of the presence of T_{reg}/T_H17 cells. This result is consistent with previously described anti-inflammatory effects of SCFA (*8*).

Notably, the only significantly increased cytokines were the T_{reg}/T_H17-related molecules TGF-β2 and 3, IL-17F, and IL-21 in the apical compartments of the PD MPSs but not PD-C. SCFA have been shown previously to increase TGF-β and IL-17 production of resting T_{reg} and T_H17 CD4 T cells (*8*). A greater number of measured analytes were significantly altered in the interactions with the PD than with the PD-C MPSs, which indicates greater susceptibility of PD MPS to the presence of SCFA—particularly in the interaction with T_{reg}/T_H17 cells.

SCFA did not significantly alter the release of αSyn in either the apical PD-C or the PD cerebral MPS (Fig. 4D); however, NSE and GFAP were significantly reduced in the apical PD MPS during interaction without T_{reg}/T_H17 cells. Although not significantly, it appears that transglutaminase 2, an enzyme involved in protein cross-linking in PD (*40*), was universally increased in the interactions of the PD MPS as compared to PD-C while UCHL1, an important neuron-specific enzyme shown to be protective against protein degradation (*41*), seemed to be reduced in the PD MPSs. SCFA significantly reduced DJ-1 release (known to inhibit αSyn aggregation) in PD but not PD-C MPSs in the presence of T_{reg}/T_H17 cells.

Interaction with SCFA increases pathology-associated transcriptomic changes in PD but not PD-C MPSs

While the analysis of inflammatory signaling molecules indicated a reduced state of immune activation during interactions in the presence of SCFA in both PD and PD-C conditions, the data also suggested the PD MPSs to be more susceptible to alterations by SCFA with additional impact on release of neuronal biomarkers (Fig. 4D). Therefore, we investigated differences in gene expression individually in PD-C as well as PD MPSs in interactions with SCFA, first without T_{reg}/T_H17 cells (Fig. 5A) and next in their presence (Fig. 5B).

Transcriptomic analysis of the PD-C MPSs among the interactions with SCFA and in the absence or presence of T_{reg}/T_H17 cells showed enrichment in beneficial pathways associated with glial cell differentiation (astrocytes and microglia), biogenic amine synthesis regulating production of the neurotransmitters dopamine and serotonin (*42*), dopaminergic neurogenesis, and G protein signaling pathways (Fig. 5, A and B). G protein receptor GPR40 is a fatty acid receptor important not only for nutrient sensing but also for normal brain development as well as maintaining proper neuronal function (*43*).

In contrast, SCFA effects on the PD cerebral MPS exhibit different mechanisms on the transcriptional level. The most significantly up-regulated pathways in SCFA-exposed PD MPSs were pathways associated with cytoplasmic ribosomal proteins (Fig. 5, A and B). While the involvement of the ribosomal protein machinery in the pathology of NDs is poorly understood, some preliminary studies link the increase of certain ribosomal protein genes to advanced PD [although this is disease stage and site specific (*44*)]. Moreover, SCFA increase the stress unfolded-protein response mediated through heat shock factor 1. Concurrently, pathways related to spinal cord injury were up-regulated in PD MPSs exposed to SCFA during physiomimetic interaction, which, according to WikiPathways, is an umbrella term encompassing increased activation and proliferation of astrocytes and microglia that results in scarring and reduced axonal regeneration, although, to a smaller degree, pathways associated with Alzheimer's disease—another ND associated with protein misfolding and aggregation—were up-regulated under both the presence of T_{reg}/T_H17 cells and their absence after exposure to SCFA.

Comparison of log_2 fold changes and significance of DGE among all conditions indicated greater sensitivity of PD cerebral MPSs to SCFA than PD-C cultures regardless of presence or absence of T_{reg}/T_H17 cells. This finding confirmed the previous observation of greater cytokine/chemokine reduction in PD MPSs by SCFA (Fig. 5C). In a direct comparison of transcriptional changes between SCFA-treated PD-C and PD cerebral MPSs during gut-liver-brain interaction in the presence of T_{reg}/T_H17 cells, significant differences in transcription were observed (Fig. 5D). Pathways associated with increased metabolism and neurogenesis are enriched in the PD-C MPSs in the presence of SCFA and T_{reg}/T_H17 cells over the PD MPS while again pathways related to cytoplasmic ribosomal proteins, mevalonate metabolism, and microglial activation are enriched in the PD MPSs (Fig. 5E).

This finding led us to further characterize other in vitro conditions (e.g., PD or PD-C cerebral MPSs in isolation or in interaction with gut and liver, and with or without T cells and/or SCFA) with respect to expression of certain genes that are known to be under- or overexpressed in patients with PD in vivo (Fig. 5F), to discern whether any of the in vitro conditions were more closely associated with known trends in patients. The condition most resembling the in vivo trends is the physiomimetic interaction with T cells and SCFA. Under both conditions, genes encoding αSyn (SNCA) and tyrosine hydroxylase (TH), which is responsible for catalyzing creation of dopamine, were underexpressed in the PD MPSs while genes related to protein translation (PABPC1), breakdown (SERPINA3), and microglia activation (CD163) were increased. These differences were pronounced at a greater fold change and statistical significance in the presence of T_{reg}/T_H17 cells and SCFA. Moreover, during this interaction, genes associated with disease-associated microglia (DAM) (*45*), particularly TREM2-dependent stage 2 DAM, were significantly increased by the presence of T_{reg}/T_H17 cells and SCFA as compared to the PD-C MPSs under the same conditions. DAM represent microglia associated with pathologic lesions in NDs (*46*).

SCFA induce transcriptomic changes unique to PD MPSs in the presence and absence of CD4⁺ T_{reg}/T_H17 cells

A number of inflammatory cytokines during interaction with and without circulating T_{reg}/T_H17 cells were reduced by SCFA, yet, at the same time, SCFA led to enrichment of pathology-related pathways under both conditions (Figs. 4 and 5) in the PD cerebral MPS but
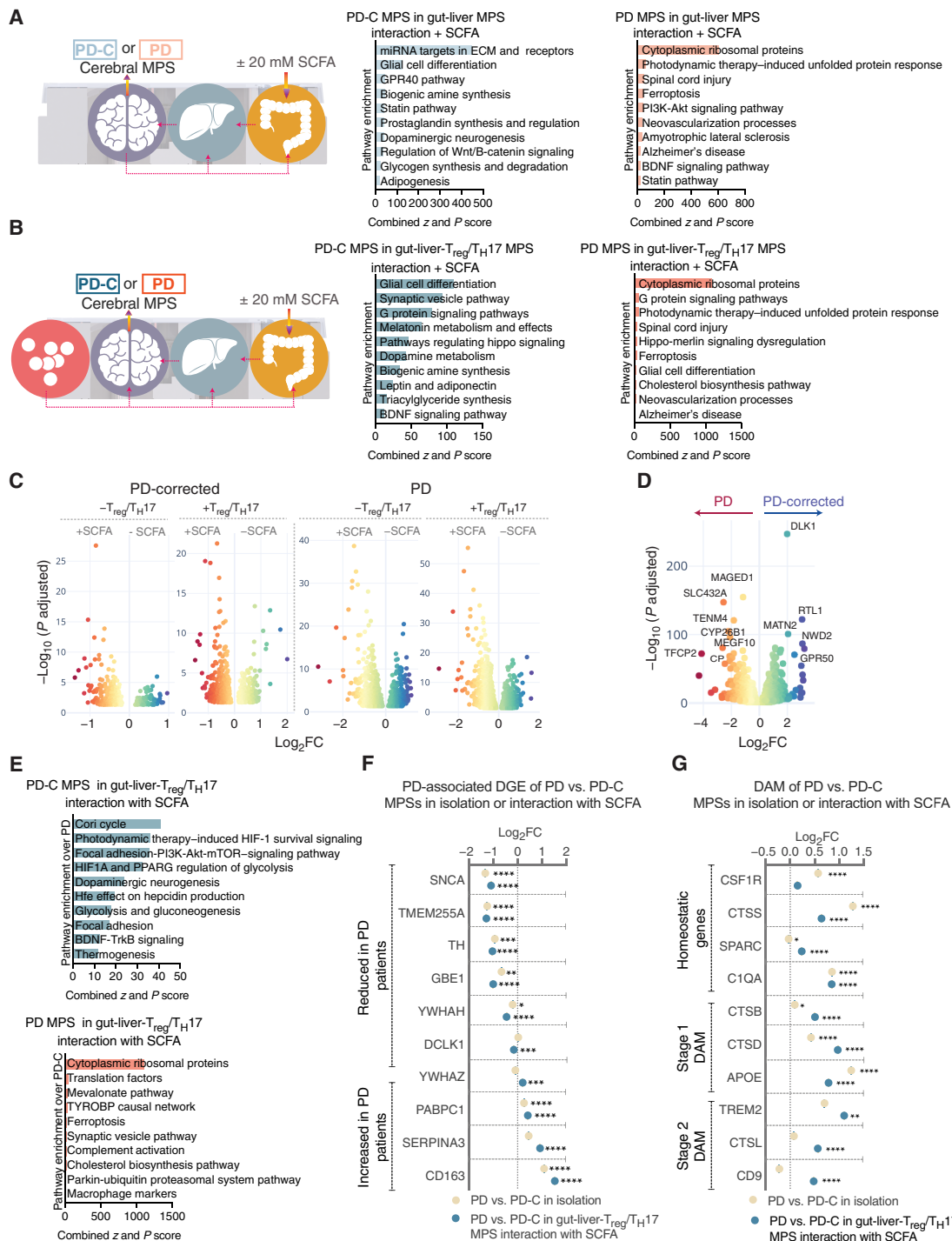
Fig. 5. SCFA increase pathology-related transcriptomic changes in PD MPSs. (**A**) Left: Schematic representation of the interaction condition. Right: Comparison of enriched pathways based on WikiPathways between SCFA-exposed and non-exposed PD-C (left) as well as PD MPSs (right) in interactions with the gut and liver MPSs. (**B**) Left: Schematic representation of the interaction condition. Right: Comparison of enriched pathways based on WikiPathways between SCFA-exposed and non-exposed PD-C (left) as well as PD MPSs (right) in interactions with the gut and liver MPSs as well as circulating $T_{reg}/T_{H}17$ cells. (**C**) Volcano plots of differentially expressed genes in control PD-C and PD cerebral MPSs across all interaction conditions in the presence (red) or absence (blue) of SCFA. (**D**) Volcano plot of DGE in SCFA-exposed PD cerebral MPSs (red) over PD-C control MPSs (blue) during gut-liver-brain interactions in the presence of circulating $T_{reg}/T_{H}17$ cells and SCFA. (**E**) Pathway enrichments based on DGE shown under (**D**) in SCFA-exposed control PD-C cerebral MPSs (top) as compared to SCFA-exposed PD MPSs (bottom) according to WikiPathways. Pathways are ranked based on a combined z and P value score. (**F**) DGE of PD-associated genes comparing PD and PD-C MPSs in isolation or interaction with $T_{reg}/T_{H}17$ cells and SCFA. Interaction significantly increases the in vivo–like expression of PD-associated genes. (**G**) DGE of disease-associated microglia (DAM)–associated genes comparing PD and PD-C MPSs in isolation or interaction with $T_{reg}/T_{H}17$ cells and SCFA where the interaction in the presence of $T_{reg}/T_{H}17$ cells significantly increases expression of DAMs. (A to G) Data represent averages of three replicates after a 4-day interaction. Significance is indicated as $*P < 0.05$, $**P < 0.001$, $***P < 0.0001$, $****P < 0.00001$.

not the control PD-C MPS. We next investigated universal SCFA-specific transcriptomic changes occurring in both the presence and absence of CD4$^+$ T cells in PD versus PD-C MPSs when they were in interaction with gut and liver MPSs. We identified 359 uniquely up-regulated genes in PD MPSs when they were in interaction with gut and liver MPSs regardless of the presence or absence of T_{reg}/T_H17 cells, while 33 genes were universally up-regulated in the PD-C MPSs by SCFA (Fig. 6A). Similarly, 303 genes were universally down-regulated in the PD MPSs and 5 in the PD-C SCFA-exposed MPSs. Analysis of gene expression in all cerebral MPSs (regardless of genotype or presence of CD4$^+$ T cells) showed that SCFA universally increased metabolic pathways associated with lipid metabolism as previously reported (47), increased pathways of acetylcholine synthesis, and reduced expression of pathways associated with immune activation in a manner consistent with the reduced concentration of inflammatory cytokines (Fig. 6B).

We next identified universally enriched (Fig. 6C) and down-regulated pathways (Fig. 6D) exclusively in the PD MPSs. SCFA specifically increased expression of genes related to cytoplasmic protein processing including cytoplasmic protein complex binding, transport, metabolism, and responses to unfolded protein with responses to metal ions based on GO Molecular Function (GO MF) and Biological Process (GO BP). Moreover, analysis based on Kyoto Encyclopedia of Genes and Genomes and WikiPathways indicated a strong up-regulation of pathways regulating silencing of ceruloplasmin. Ceruloplasmin is vitally important for iron transport and prevention of iron accumulation, and mutations in the ceruloplasmin encoding gene have been found to be associated with increased iron accumulation in patients with PD (48). The A53T αSyn mutation has explicitly been linked to increased iron-dependent aggregation and toxicity (49) due to αSyn's strong affinity for both ferric and ferrous iron with both forms of iron accelerating αSyn aggregation (50). Concurrently, pathways associated with ferroptosis were increased.

On the other hand, SCFA universally reduced pathways involved in glutamate receptor activity, general neurogenesis, and chromosome organization. Moreover, SCFA reduced pathways of protein SUMOylation. Posttranslational modification of αSyn via small ubiquitin-like modifier (SUMO) proteins is necessary to prevent αSyn aggregation, and SUMOylation of DJ-1 is critical for its full function (35).

Together (Fig. 6E), our findings show interaction of PD-C cerebral MPSs with the gut-liver axis to increase expression of pathways related to (i) maturation of neurons, microglia, and astrocytes; (ii) immune function; and (iii) neuronal function. Addition of SCFA further increased lipid metabolism–related pathways in all cerebral MPSs regardless of phenotype. The observed SCFA-induced changes appeared to benefit the PD-C cerebral MPSs under all conditions while the opposite seems to be true for the PD MPSs in the presence or absence of T_{reg}/T_H17 cells. Under both interaction conditions, SCFA reduced pathways related to general neurogenesis and increased expression of genes related to neurodegenerative pathology. While these preliminary results paint an interesting hypothesis, further work using a variety of different donors and cell lines will speak of the universality of our findings in terms of both donor specificity and specificity of these results regarding the underlying cause of proteinopathies.

DISCUSSION

Multifactorial NDs remain one of the biggest medical challenges of our time, because both environmental and genetic factors are inter-twined, obscuring causality. While most of our current knowledge about PD comes from valuable animal experimentation and human clinical data, the overwhelming disease complexity on a whole organismal level is a roadblock to progress in its own right. With the advance of human ex vivo modeling of organ-organ interactions, previously inaccessible possibilities arise in recreating complex aspects of human disease etiology under defined and controlled conditions (9).

At present, in vitro models insufficiently recapitulate organ-organ and organ-immune interactions required for representative modeling related to gut-liver metabolism, immunity, and complex cerebral biology (51, 52), but a number of technologies have been developed for the coculture of various MPSs that represent important stepping stones in the evolution of multiorgan-interacting platforms (52, 53). Drug metabolism and toxicology have been mainstay applications of MPS technologies (51, 52), with emerging applications in modeling diseases necessitating incorporation of more complex organ-level phenomena (8, 11, 14). Multiorgan pharmacokinetics and toxicity have been investigated by pipetting discrete aliquots of media between individual MPSs (53, 54) and by interconnecting individual MPSs fluidically on a platform (55), an approach that is also being applied to disease modeling (8, 56). However, extended (48+ hours) coculture with innate immune cells and concomitant analysis of inflammation responses have not been described. Acute trafficking of circulating immune cells through an endothelial or epithelial barrier has been studied in individual MPSs using once-through flow (15), but a significant barrier to extended coculture of circulating immune cells with interconnected MPS is the need for pumps that are both safe for circulating immune cells and compatible with lipophilic culture medium components, including drugs (i.e., pump materials must exclude PDMS).

Our conceptual and experimental model of continuous and prolonged interactive immune-metabolic cross-talk between organ systems represents a significant advance in modeling the human gut-brain axis in the context of NDs in vitro. We have created a human gut-liver-cerebral physiomimetic system that incorporates cells of both the innate and adaptive immune system. Using this approach and advanced genetic tools, we were able to observe increased maturation of hiPSC-derived neurons, astrocytes, and microglia on the transcriptomic level. Using hiPSCs from a donor with familiar PD carrying the A53T mutation, we could partially recreate known clinical manifestations of familial PD that includes several markers indicative of αSyn aggregation, previously reported changes in lipid metabolism, and increase in pathways related to neuronal pathology. However, it is important to note that PD encompasses a great number of different pathological changes that are not restricted only to neurons and the brain; hence, the here presented system mimics only a subset of known disease hallmarks. Moreover, PD is a slow-progressing disease that develops over decades, which is a considerable challenge from the perspective of disease modeling, both in vitro and in vivo. Currently, we can only perform comparative exposure studies over relatively short time frames compared to the time frames for disease development. Whereas some individual cerebral MPSs have been maintained in culture for over 5 months and liver MPS for weeks (12), the duration of the experiments here was limited in the longevity of the gut mucosal barrier. Gut epithelia differentiate rapidly when cultured in a format lacking continuous stimulation from the basal compartment by niche factors that maintain the stem cell compartment (57). These factors were not used as they are deleterious to the
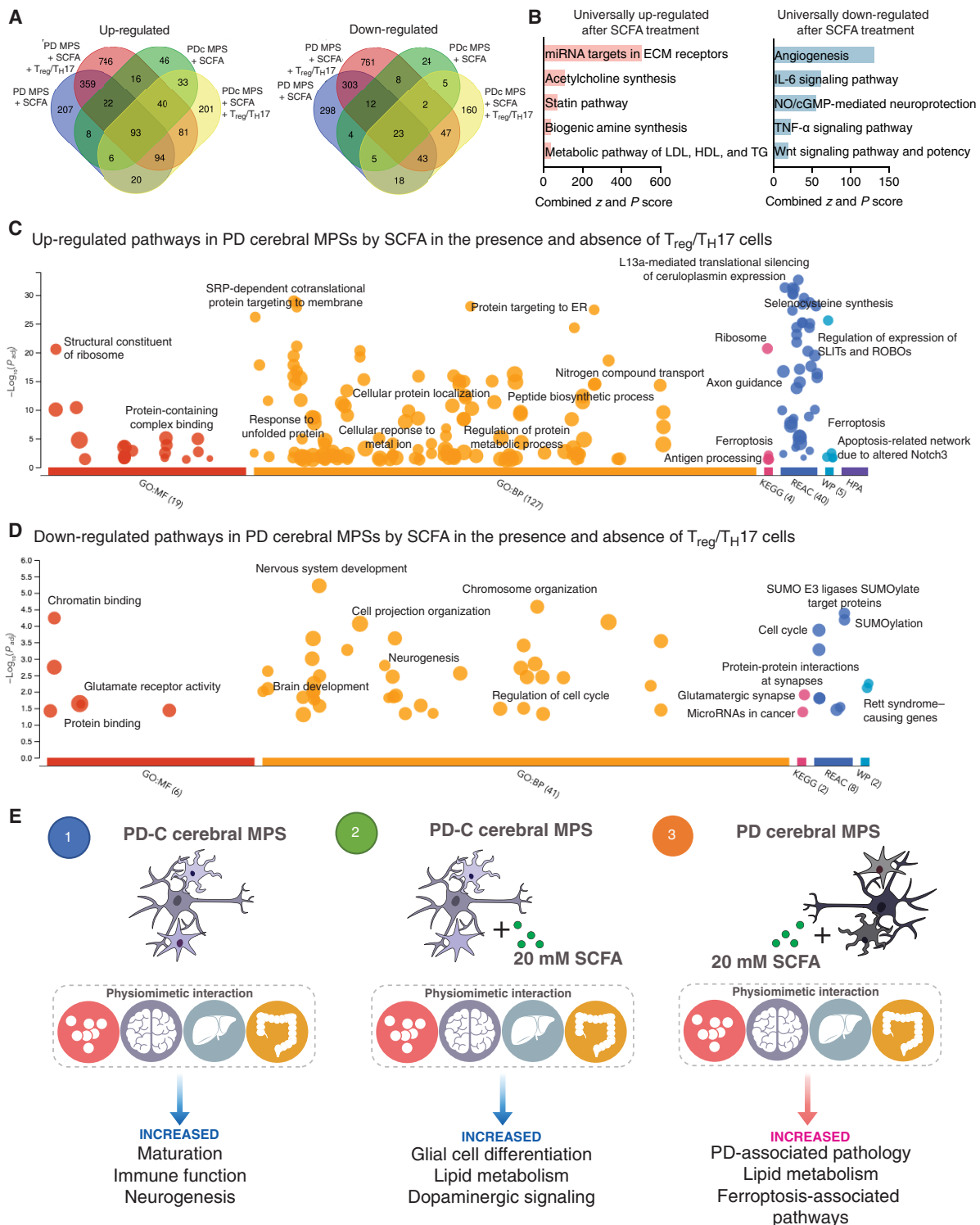
Fig. 6. PD MPS-unique transcriptional changes during interaction with SCFA. (**A**) Venn diagram showing number of unique or shared DGE among SCFA-exposed PD and PD-C MPSs during interaction with the gut and liver in the presence or absence of circulating T_{reg}/T_H17 cells. Left: Up-regulated genes, right: down-regulated genes. On the basis of the number of altered genes, SCFA affect PD MPSs to a greater extent than PD-C MPSs. (**B**) Pathway enrichments based on DEG shown under (A) universally in all cerebral MPSs, regardless of genotype or the presence of T_{reg}/T_H17 cells, according to WikiPathways database. Pathways are ranked on the basis of a combined z and P value score. (**C**) Up-regulated pathways, identified with g:Profiler, exclusively in PD cerebral MPSs after interaction and the exposure to SCFA regardless of the presence of T_{reg}/T_H17 cells. (**D**) Down-regulated pathways, identified with g:Profiler, exclusively in PD cerebral MPSs after gut-liver interaction and the exposure to SCFA regardless of the presence of T_{reg}/T_H17 cells. (A to D) Data represent averages of three replicates after a 4-day interaction. (**E**) Schematic summary of unique and universal effects of SCFA during interaction with the PD-C and PD cerebral MPSs.

other MPSs. Tissue-engineering approaches that combine the niche factor–producing stromal cells with epithelial cells in a crypt-lumen configuration are needed to create a long-lived gut mucosa, and we speculate that several biomaterials and microfabrication technologies recently described for gut mucosal barrier culture might soon be combined to this end (57, 58).

Our work shows that interaction of corrected cerebral MPSs with the gut and liver MPSs and circulating T_{reg}/T_H17 leads to increased expression of neuronal, astrocyte, and microglial homeostatic genes as well as metabolic pathways related to glycolysis and cholesterol synthesis. Moreover, the interaction increased dopamine receptor–mediated signaling, axon guidance, and serotonin and oxytocin signaling in interacting cerebral MPSs. Inclusion of both innate and adaptive immune cells in the physiomimetic system resulted in cytokine/chemokine values closer to reported values in human plasma and CSF. Future experiments will be aimed at exploring changes in functionality of the individual cell types involved in this study. These experiments can be coupled to advanced models of heterologous cellular cytokine cross-talk and network models of metabolism to further illuminate immune-metabolic cross-talk with organ systems (59–61).

Exacerbated neuronal damage is accompanied by inflammatory responses in vivo, where a question remains whether inflammation itself is a primary driver of PD pathology. Addition of SCFA in the gut-liver-brain interaction led to a marked decrease in inflammatory mediators in interactions with and without T_{reg}/T_H17 cells. Gastrointestinal symptoms often precede motor manifestations of PD (62), and in mouse models of PD, SCFA were implicated in early onset of PD (1), yet paradoxically, a study comparing the colonic microbiota of patients with PD with those of healthy controls has identified a reduced frequency of SCFA-producing bacterial phyla among the PD cohort (62). This contradiction might be explained by the context-dependent modulatory action of SCFA that might depend on the disease stage or genetic background. SCFA can dampen inflammation and promote differentiation of tolerance inducing $CD4^+$ T_{reg} cells (63), yet exacerbate proinflammatory programs of activated $CD4^+$ (8, 39) and $CD8^+$ T cells (64). However, in the physiomimetic interaction of SCFA (albeit in the absence of a live microbiome) and PD cerebral MPSs carrying the A53T mutation, in both the presence and absence of T_{reg}/T_H17 cells, SCFA lead to enrichments in PD-associated pathways and changes on the global gene expression indicative of neuronal damage. This might be due to inflammation-independent modulatory properties of SCFA related to lipid metabolism. The mevalonate pathway was the most enriched pathway when comparing the metabolomic profile of PD versus PD-C MPSs in isolation, which is an essential pathway required for cholesterol synthesis and a target of statins—a class of cholesterol-lowering drugs (65). Studies report both disease-improving and disease-exacerbating effects of statins in general, and a consensus has yet to be achieved (66). The brain is a highly lipid-rich organ where both cholesterol accumulation and monounsaturated fatty acid metabolism have been linked to neurotoxicity; hence, an urgent need exists to further clarify involvement of fatty acid metabolism in PD (67).

Last, a limitation of the current study and many other in vitro models of NDs, such as 2D single-cell type cultures or brain organoid-based models, is the absence of a functional in vitro BBB. Although significant progress in modeling the neuro-vascular unit has been made and a number of in vitro models of the BBB have been developed on the basis of iPSCs, cell lines, or human umbilical vein endothelial sources (54, 68, 69), in vivo–like function of the barrier is notoriously difficult to achieve. This stems from the fact that (i) the BBB is not composed of one single cell type but rather requires the interplay of a number of cells with varying ratios to achieve in vivo functionality, (ii) they are not static in their physiological behavior but highly dynamic in terms of permeability as well as the receptors and transporters they express as a response to changes in environment, and (iii) vascular barriers are not the same throughout the human body but rather specific. As a result, in vitro BBBs lack well-defined and accepted benchmarks and can present misleading biological features of a multi-MPS system (69, 70). Cytokines, SCFA, and other microbial metabolites pass the barrier (3, 53); hence, we chose to compare interaction of MPSs, immune cells, and SCFA laterally between PD and PD-corrected MPSs in the absence of an in vitro BBB. While important differences exist between the response of the PD and PD-corrected cerebral MPSs to SCFA, this work can serve as a reference point without the inclusion of an in vitro BBB in which future models with an in vivo–like BBB can be evaluated.

In the gut, the vascular barrier is involved in inflammation associated with microbial antigens, a phenomenon we deliberately separate from that of microbial small-molecule metabolites and hence was not included in the present study. The epithelial barrier is the major gate to the systemic circulation for metabolic products, such as SCFA, and cytokines analyzed here. Similarly, the highly fenestrated liver sinusoidal endothelial cells are antigen-presenting cells that are involved in response to bacterial antigens and modulate immune cell trafficking (71) but become a significant barrier to hepatocyte uptake of nutrients only under cirrhotic conditions outside the scope of those studied here.

In our lateral comparison of PD and PD-C MPSs during interaction, even without a BBB, we were able to identify significant links between SCFA and the PD cerebral MPSs. These were unique to the PD genotype and were not observed among MPSs with the corrected A53T mutation. Notably, pathways related to ferroptosis were uniquely increased in PD but not PD-C MPSs during interaction with SCFA, regardless of the presence of T_{reg}/T_H17 cells and the reduction in inflammatory cytokines. This might suggest a lipid metabolism–related, rather than immune-related link between SCFA and PD neuronal pathology in vitro. Ferroptosis is a form of regulated cell death where iron-dependent accumulation of lipid hydroperoxides leads to cell death (72). Iron, phospholipids, and fatty acid metabolism increase the cells' susceptibility to ferroptosis (73). Evidence of ferroptosis as a cause of death in dopaminergic neurons in PD is mounting and increased interest exists in the connection between protein misfolding, ferroptosis, and lipid metabolism that warrants further investigation (74).

Last, our proof-of-concept physiomimetic study indicates that interaction of cerebral MPSs with gut and liver MPSs increases expression of genes associated with maturation of neurons, astrocytes, and microglia—a feature notoriously hard to achieve in in vitro models of the brain. Further verification with additional cell lines representing different patient origins will be useful for extending our biological findings, but our current study illustrates how key questions can be defined and combined with an experimental framework, representing an essential first step in this direction. Our work adds credence to the growing promise of physiomimetic technologies to serve as tools for hypothesis generation and mechanistic confirmation

as well as a capability to supplement current preclinical approaches in neurodegenerative research.

MATERIALS AND METHODS
Gut MPSs
Gut organoids
The colon organoids HC176 of nondiseased tissue used in this study were established and maintained as previously described (*75*) by the Harvard Digestive Disease Center. Endoscopic tissue biopsies were collected from the ascending colon of de-identified individuals at Boston Children's Hospital upon the donors' informed consent. Methods were carried out in accordance to the Institutional Review Board of Boston Children's Hospital (protocol no. IRB-P00000529). We digested the tissue in 2 mg ml^{-1} collagenase I (StemCell, catalog no. 07416) for 40 min at 37°C followed by mechanical dissociation, and isolated crypts were resuspended in growth factor–reduced Matrigel (Corning, catalog no. 356237) and polymerized at 37°C. Organoids were cultured in expansion medium (EM) consisting of Advanced Dulbecco's modified Eagle's medium (DMEM)/F12 supplemented with L-WRN conditioned medium (65% v/v; American Type Culture Collection, catalog no. CRL-3276), Glutamax (2 mM; Thermo Fisher Scientific, catalog no. 35050-061), Hepes (10 mM; Thermo Fisher Scientific, catalog no. 15630-080), penicillin/ streptomycin (Pen/Strep) (Thermo Fisher Scientific, catalog no. 15070063), murine epidermal growth factor (EGF) (50 ng ml^{-1}; Thermo Fisher Scientific, catalog no. PMG8041), N2 supplement (Thermo Fisher Scientific, catalog no. 17502-048), B-27 Supplement (Thermo Fisher Scientific, catalog no. 17502-044), human [Leu15]-gastrin I (1 nM; Sigma-Aldrich, catalog no. G9145), *N*-acetyl cysteine (500 µM; Sigma-Aldrich, catalog no. A9165-5G), nicotinamide (10 mM; Sigma-Aldrich, catalog no. N0636), thiazovivin (2.5 µM; Tocris, catalog no. 3845), A83-01 (500 nM; Tocris, catalog no. 2939), SB202190 (10 µM; PeproTech catalog no. 1523072), prostaglandin E2 (5 nM; StemCell catalog no. 72192) at 37°C and 5% CO_2. Organoids were passaged every 7 days by incubating in Cell Recovery Solution (Corning, catalog no. 354253) for 40 min at 4°C, followed by mechanical dissociation and reconstitution in fresh Matrigel at a 1:3 to 4 ratio.

Epithelial monolayers on Transwell inserts
Colon organoids were collected at days 7 to 9 after passaging. Cell Recovery Solution was used for 40 min at 4°C to dissolve Matrigel, followed by incubation of organoids in Trypsin/EDTA (Thermo Fisher Scientific, catalog no. 12605036) at 37°C for 5 min. Next, organoids were mechanically dissociated into single cells, resuspended in EM without nicotinamide, and seeded onto type I collagen (50 µg/ml)–coated 12-well 0.4-µm pore polyester Transwell inserts (Corning, 3493) at a density of 3×10^5 cells per Transwell. After 3 to 5 days of incubation, monolayers were confluent and we initiated differentiation as described previously (*8*). For differentiation, apical medium was replaced with Advanced DMEM/F12 plus Hepes, Glutamax, and Pen/Strep and basolateral media with differentiation medium, which is EM without L-WRN conditioned medium, nicotinamide, prostaglandin E2, SB202190, and thiazovivin, but supplemented with human recombinant noggin (100 ng ml^{-1}; PeproTech, catalog no. 120-10C) and 20% R-spondin conditioned medium (Sigma-Aldrich, catalog no. SCC111). Monolayer integrity was monitored with transepithelial electrical resistance (TEER) measurements, which were performed using the EndOhm-12 chamber with an EVOM2 meter (World Precision Instruments). Monolayers were used for further experimentation at days 7 to 9 after seeding.

Coculture of epithelial monolayers with dendritic cells and macrophages (gut MPS)
Gut MPSs were prepared by seeding human monocyte-derived dendritic cells and macrophages, as the innate immune component of the gut MPS, on the basolateral side of Transwell membranes that have differentiated epithelial monolayers on the apical side as described before (*8*). The monocytes were isolated from Leuko Pak PBMCs (StemCell, catalog no. 70500) using the EasySep Human Monocyte Enrichment Kit without CD16 depletion (StemCell, catalog no. 19058). We differentiated macrophages in RPMI 1640 medium (Gibco) supplemented with 10% fetal bovine serum (FBS), 1× Glutamax, and Recombinant Human M-CSF (100 ng/ml; BioLegend, catalog no. 574804). Dendritic cells were differentiated in RPMI 1640 medium (Gibco) supplemented with Pen/Strep, 10% heat-inactivated FBS, 1% MEM Non-Essential Amino Acid Solution (Gibco), 1% Glutamax, GM-CSF (100 ng/ml; BioLegend, catalog no. 572903), Recombinant human IL-4 (70 ng/ml; BioLegend, catalog no. 574004), and retinoic acid (10 nM; Sigma-Aldrich, catalog no. R2625-50MG). After 7 days of differentiation (at day 8 after epithelial cell seeding), dendritic cells and macrophages were harvested using TrypLE Express (Gibco) and seeded onto the basal side of the Transwells, 2.5×10^4 cells per population per Transwell. Gut MPSs with TEER greater than 200 ohm·cm^2 were considered acceptable for experimentation and were integrated onto the 3XGLB platform for interaction studies. During all experiments, the gut MPSs were maintained in serum-free apical medium consisting of Advanced DMEM/F12 with or without the SCFA, sodium acetate (12 mM), sodium propionate (4 mM), and sodium butyrate (4 mM) from Sigma-Aldrich.

Common media
The basal gut compartment and the liver and cerebral MPS compartments that were fluidically linked to systemic circulation on the 3XGLB were fed with serum-free CM that contained William's E medium (Thermo Fisher Scientific, catalog no. A1217601), 4% Cell Maintenance Supplement Pack (Thermo Fisher Scientific, catalog no. CM4000), IL-2 (50 IU/ml; R&D Systems, catalog no. 202-IL), 100 nM hydrocortisone, 5 mM glucose, 800 pM insulin, and 0.5% Pen/Strep. Experiments here and throughout the entire work were conducted in modified culture medium that had previously been tailored for physiological responses of the human liver MPS, in which the high nonphysiological concentrations of cortisol and insulin, typically used to maintain CYP450 levels in primary hepatocyte cultures, were reduced to concentrations within the physiological range (*12*, *13*).

Liver MPSs
Preparation of the liver MPSs was performed as described previously. Single-donor human primary hepatocytes were obtained from BioIVT (lot AQL; 63-year-old male), and Kupffer cells, as the innate immune component of the liver MPSs, were purchased from Thermo Fisher Scientific (catalog no. HUKCCS; 29-year-old male). Both cell types were seeded on liver scaffolds that are 0.25-mm polystyrene discs perforated with 301 channels (diameter = 0.3 mm) (*14*). Scaffolds were soaked in 70% EtOH for 15 min, washed twice with phosphate-buffered saline (PBS), and coated with rat tail collagen I (30 µg/ml) in PBS for 1 hour at room temperature (RT). Collagen-coated scaffolds were air-dried and then punched into the 3XGLB platforms for interaction experiments. On the basis of our previous work (*8*),

hepatocytes and Kupffer cells were thawed in Cryopreserved Hepatocyte Recovery Medium 5 days before interaction experiments (Thermo Fisher Scientific, catalog no. CM7000), centrifuged at $100g$ for 8 min, and seeded in a 10:1 ratio on to the scaffold, $6 \times 10^5 : 6 \times 10^4$ cells per well, in hepatocyte seeding medium (Thermo Fisher Scientific, catalog no. A1217601) with 5 mM glucose, 5% FBS, 100 nM hydrocortisone, and an in-house supplement cocktail equivalent to Gibco Cocktail A (Thermo Fisher Scientific, catalog no. CM3000; but with only 200 to 800 pM insulin) and cultured under flow at 37°C. After 1 day, the medium was changed to hepatocyte maintenance medium [William's E medium with 5 mM glucose, 100 nM hydrocortisone, and an in-house supplement cocktail equivalent to Gibco Cocktail B (Thermo Fisher Scientific, catalog no. CM4000) but with only 200 to 800 pM insulin] and changed at day 3. At day 5 after seeding, the medium was changed to CM + 25UI IL-2, and the interaction studies with the gut and cerebral MPSs had begun. The CM was also added to the control LiverChip. To evaluate the physiological status of the liver, samples from all compartments but the apical gut MPS (i.e., liver, directly above the scaffold; basal gut MPS; and mixer) were taken at every medium change (every 48 hours) and assayed for albumin via enzyme-linked immunosorbent assay (Bethyl Laboratories, catalog no. E80-129).

Cerebral MPSs

The cerebral MPSs were established as cocultures of neurons, astrocytes, and microglia seeded on 24-well Transwells. All three cell types are differentiated from the same donor cell lines. Cells of the PD cerebral MPS (PD cerebral MPS) are differentiated from hiPSCs stemming from fibroblasts of a patient with early onset of PD due to an A53T point mutation in exon 3 of the αSyn gene (76). To control for the mutation, we have used hiPSCs from the same donor but with the corrected mutation for our control cerebral MPS (PD-C cerebral MPS). hiPSCs carrying the αSyn mutation were reprogrammed using doxycycline-inducible and Cre-recombinase–excisable lentiviral vectors. Both progenitor cell lines and methodology were published and extensively described previously (5). The three cell types in coculture were allowed to attach and form a 3D network of protrusions on the microporous membranes over the course of at least 24 hours before being moved onto the 3XGLB platform for interaction studies.

Differentiation of neurons/astrocytes

Both hiPSC carrying the A53T point mutation (PD phenotype) and hiPSC with the corrected A53T mutation (corrected phenotype) were first differentiated into neural progenitor cells (NPCs). Cells were treated with collagenase for 30 min and collected into 15-ml Falcon tubes containing hES media. Following two washes with hES media and one wash with PBS$^{-/-}$, cells were treated with Accutase for 10 min and broken into single cells. The cell suspension was filtered through a 40-μl filter with Hanks' balanced salt solution (HBSS)/bovine serum albumin (BSA) 0.1% into a 50-ml Falcon tube. A total of 5×10^6 cells per well were plated on a six-well plate with neuroglial differentiation (NGD) media (see Table 1) that contained 2.5 μM dorsomorphin, fibroblast growth factor (FGF; 10 ng/ml), insulin (1:500), and RI (1:1000). Medium was changed daily for 11 to 14 days. Three days after rosette formation, cells were passaged in a 1:1 ratio. For final differentiation, 2×10^6 NPCs per well were seeded on a six-well plate in NGD media. Cells were differentiated for 4 weeks with media changes every 3 days.

Table 1. NGD media formulation.

Reagent	Volume
Gem21 without vitamin A	5 ml
Neuroplex N2	2.5 ml
Albumax I	1 g
NaCl 5 M	5 ml
Sodium pyruvate 100×	5 ml
Pen/Strep	5 ml
Glutamax	5 ml
Biotin (5 mg/ml in 1 M NaOH)	0.35 μl
Ascorbic (100 mM stock)	50 μl
Lactic syrup (60%)	100 μl
Neurobasal media	500 ml

Differentiation of microglia

Microglia were differentiated from iPSCs using a previously published protocol (77). Briefly, hiPSCs were adapted to feeder-free conditions on Matrigel (Thermo Fisher Scientific CB40234) in mTesr media (StemCell Technologies 85850). Once stably adapted, iPSC colonies were plated at low density on low–growth factor Matrigel (Thermo Fisher Scientific CB40230) in T75 flasks in mTesr media. Once colonies reached 1 mm in diameter, flasks underwent the following media changes outlined in step 1 through step 4: (step 1) mTesr media containing BMP4 (80 ng/ml; PeproTech 120-05ET) for 4 days; (step 2) Stempro media (Life Technologies 10639011) with FGF (25 ng/ml; Life Technologies PHG0263), SCF (100 ng/ml; PeproTech 300-07), and vascular EGF (80 ng/ml; PeproTech 100-20), for 2 days; (step 3) Stempro media with IL-3 (50 ng/ml; PeproTech 200-03), Flt3 (50 ng/ml; PeproTech 300-19), M-CSF (50 ng/ml; PeproTech AF-300-25), TPO (5 ng/ml; PeproTech 300-18-500u), and SCF (50 ng/ml) for 8 days; and (step 4) Stempro media with M-CSF (50 ng/ml), Flt-3 (50 ng/ml), and GM-CSF (25 ng/ml; PeproTech 300-03). Myeloid precursor cells started to be released into suspension several days after beginning step 4. Following 4 to 7 days in step 4, myeloid precursors were collected and plated for microglial differentiation. Myeloid precursors were plated on six-well Primaria plates (VWR 62406-455) at 1×10^6 per well in the following media: Neurobasal (Life Technologies 21103049) supplemented with 1% Gem21 B27 (Gemini BioProducts 400161), Neuroplex 0.5% N2 (Gemini BioProducts 400163), 0.2% Albumax I (Life Technologies 11020021), 50 mM NaCl (Sigma-Aldrich), 1× Pyruvate (Life Technologies 11360070), 1× Pen/Strep (Life Technologies), and 1× Glutamax (Life Technologies 35050061), supplemented with cytokines TGF-β1 (25 ng/ml; PeproTech 100-21-500 μg), M-CSF (12.5 ng/ml), and IL-034 (100 ng/ml; PeproTech 200-34). Cells were differentiated into microglia for 2 weeks. To generate Transwells, microglia were collected using a 10-min incubation in 2 mM EDTA (Life Technologies AM9260G) and combined with isolated neurons at a ratio of 1 microglial cell to 10 neurons.

PD and PD-corrected cerebral MPSs

After differentiation neurons, astrocytes and microglia were treated with Accutase for 10 min at 37°C and collected into 15-ml Falcon

tubes with 10-ml plastic pipettes and placed in the incubator for an additional 10 min at 37°C. Cells were gently triturated 10× with a 5-ml glass pipette. Deoxyribonuclease I was added to a concentration of 0.05% followed by repeated gentle resuspension 10×. HBSS with 0.1% BSA was added to the suspension and filtered through a 40-μm mesh filter with an underlying cushion of HBSS with 4%. Cells were centrifuged at 100g for 10 min at 4°C and counted. Before seeding the cells onto 24-well 0.4-μm pore polyester Transwell inserts, the membranes were coated overnight with 0.1% polyethyleneimine (PEI) at 4°C. Neurons/astrocytes were seeded at a density of 2×10^5 per cerebral MPS with 2×10^4 microglia. During studies off-platform and during the gut-liver-brain interaction, the gut MPS had 200 μl of NGD media added to the apical compartment whereas the basal compartment contained the CM.

Human circulating CD4 T$_{reg}$ and T$_H$17 cells

Naïve CD4 T cells were used to differentiate T$_{reg}$ and T$_H$17 cells derived from the same Leuko Pak donor, a 44-year-old Caucasian female (StemCell, catalog no. 70500) as the dendritic cells and macrophages in the gut MPS. Naïve CD4 T cells were isolated with the EasySep Human Naïve CD4$^+$ T Cell Isolation Kit II (StemCell, catalog no. 17555). Cells were differentiated to T$_{reg}$s or T$_H$17 cells in RPMI 1640 medium (Gibco) supplemented with Pen/Strep, 10% heat-inactivated FBS, 1% MEM Non-Essential Amino Acid Solution, 1 mM sodium pyruvate, 1% Glutamax, 2.5% ImmunoCult Human CD3/CD28 T cell activator (StemCell, catalog no. 10971), and human TGF-β (5 ng/ml; R&D Systems, catalog no. 240-B/CF). In addition, T$_{reg}$s received IL-2 (100 IU/ml; R&D Systems, catalog no. 202-IL) and 10 nM retinoic acid (Sigma-Aldrich, catalog no. R2625-50MG), while for T$_H$17 cell differentiation, 10 ng/ml each of human IL-6 and IL-1β (R&D Systems, catalog no. 206-IL, 201-LB) were added. After 7 days of differentiation at 37°C, cells were harvested into CM and distributed in a physiological 2:1 ratio of T$_{reg}$/T$_H$17 cells among the compartments on the 3XGLB platform (total of 2.4×10^5 T$_{reg}$s and 1.2×10^5 T$_H$17 cells per interaction lane) (8). T$_{reg}$/T$_H$17 ratio in human peripheral blood varies from 0.2 to 1 in healthy individuals and total T$_{reg}$ numbers vary from 7×10^4 to 5×10^5 per milliliter. While T cells were prevented to come into direct contact with the epithelium and neurons/astrocyte/microglia grown on microporous membranes, their contact was enabled with antigen-presenting cells of the gut MPS and the liver MPS.

Immunofluorescence confocal imaging
Gut MPS
Epithelial monolayers on the apical side of Transwell membranes and macrophages/dendritic cells on the basolateral side were washed with fluorescence-activated cell sorting (FACS) buffer (PBS with 2% FBS) and stained with primary mouse anti-human CD14 (BD Pharmingen, catalog no. 347490) according to previously established protocols (8). Following a wash with FACS buffer, cells were fixed and permeabilized with a Fixation/Permeabilization kit (BD Biosciences, catalog no. 554714) and concurrently stained with an Alexa Fluor 488 secondary goat anti-mouse antibody (BioLegend, catalog no. 405319), NucBlue (Invitrogen, catalog no. 12303553), and ActinRed (Invitrogen, catalog no. 15119325). The membranes were mounted on glass slides with Prolong Diamond Antifade (Invitrogen, catalog no. 15205739) and cured for 24 hours. Images were acquired with the Zeiss LSM 880 confocal microscope at a 63× magnification and curated with the Zeiss ZEN software.

Cerebral MPS
Transwells, containing neurons, astrocytes, and microglia, were fixed in 4% paraformaldehyde (PFA) (Electron Microscopy Science catalog no. 15710) in PBS for 30 min at RT followed by washing with PBS 1× and permeabilization with 0.3% Triton (Sigma-Aldrich, catalog no. T8787-100ML) in PBS. Cells were blocked with 3% BSA (Sigma-Aldrich, catalog no. A7030-100G) in PBS for 30 min at RT. Primary antibodies used were goat anti-Iba1 (Abcam, catalog no. AB5076; 1:500), mouse anti-Tuj1 (BioLegend, catalog no. 801201; 1:1000), and rabbit anti-S100B (Agilent, catalog no. Z031129-2; 1:1000). Primary antibodies were diluted in 3% BSA + 0.1% Triton in PBS and incubated at 4°C overnight. Next day, cells were washed 3× with PBS and stained with secondary antibodies Alexa 488, 568, and 647 (Life Technologies; 1:500). Secondary antibodies were added for 2 hours at RT followed by 2× washing with PBS. Transwell membranes with the stained cells were mounted onto glass slides (VWR catalog no. 488311-703) with mounting buffer (Electron Microscopy Science catalog no. 17984-25). Images were acquired with the Zeiss LSM 710 confocal microscope at a 20× magnification, curated with the Zeiss ZEN software, and processed with Imaris 9.2.0 (Bitplane, Zurich, Switzerland).

Physiomimetic platform 3XGLB
Fabrication and assembly
We developed the underlying technology of the 3XGLB in-house as described previously (52). The 3XGLB iteration of the system was designed in CAD and commercially machined. The pneumatic plates were machined in acrylic and solvent bonded to form two-layer manifolds, while the fluidic plates were machined from monolithic polysulfone. We treated the pneumatic plates with vapor polishing and fluidic plates were cryo-deburred to remove sharp burrs. Fifty-micrometer-thick polyurethane membranes are supplied by American Polyfilm Inc. and mounted onto grip rings (Ultron Systems UGR-12) to provide uniform tension. The membranes were laser-cut to remove material around screw holes. After cutting, they were rinsed in 10% 7× solution followed by deionized (DI) water and then sterilized using ethylene oxide gas. All hardware components are reusable, except for the polyurethane membranes. Flow of media between compartments on the platform is achieved by pumping driven from outside the incubator by a microcontroller and a pneumatic solenoid manifold controlling the tubing, which is run through the back of the incubator to intermediary connectors. The system allows for safe circulation of CD4 T cells within and between compartments at high velocities and preserved T cell viability (fig. S1B). Inside the incubator, tubing is attached to the platform through valved breakaway couplings, allowing removal from the incubator for media changes and sampling. Flow rates and calibration factors can be adjusted through a graphical user interface and are sent to a customized microcontroller (National Instruments myRIO-1900) over USB or WiFi.

Operation
Sterile platforms were assembled 4 days before experimentation in a laminar flow hood. They were primed with PBS containing 1% BSA (Sigma-Aldrich, catalog no. A9576) and Pen/Strep. Pump function and tubing connections were visually confirmed by pumping from the mixer (cerebral MPS compartment) to each dry compartment and then by running the recirculation pumps backward to clear all air from the channels. We ran the platforms overnight in the incubator to passivate and confirm full operation before the addition of the gut, liver, and cerebral MPS as well as the circulating T$_{reg}$/T$_H$17 cells (8). On the day of the experiment, priming media were replaced

with serum-free CM (see the "Common media" section) with the volume of each compartment being as follows: gut MPS, 2 ml (apical 0.5 ml, basal 1.5 ml); liver MPS, 1.6 ml; and the cerebral MPS compartment, 3.1 ml (apical 0.8 ml, basal 2.3 ml) for a total recirculation volume of 5.4 ml and total system volume of 6.7 ml. The layout of the platform and flow parameters are indicated in fig. S1, but in brief, media from the basal gut compartment were distributed to the liver and, from there, to the cerebral MPS compartment. The cerebral MPS compartment serves as a mixer that re-distributes media back to the gut (75%) and liver (25%). Interaction studies were performed over 4 days with complete media changes every 48 hours. Circulating T_{reg}/T_H17 cells that were collected with the media during the 48-hour media change were returned to each original platform equally distributed among the three compartments. During the media change and at the end of the interaction studies on day 4, CM was collected from the apical and basal gut compartment, from the liver compartment above the scaffold, and from the apical and basal compartment of the cerebral MPS. Media samples were collected in low-binding tubes, supernatants were spun down at 10,000g for 5 min to remove cell debris, BSA was added to a final concentration of 0.5% (except the samples reserved for metabolomic analysis), and the samples were transferred to a −80°C freezer. Cytokine/chemokine and albumin measurements during interaction studies were performed on the media collected from the basal cerebral MPS/mixer compartment that distributes the media between the gut and liver MPSs. Each condition was performed in three biological replicates.

Multiplex cytokine/chemokine assays and analysis

We measured the cytokine/chemokine concentrations using the following multiplex assays from Millipore Sigma: MILLIPLEX MAP Human Neuroscience Magnetic Bead Panel 1 (catalog no. HNS1MAG-95k), MILLIPLEX MAP Human Cytokine/Chemokine Magnetic Bead Panel—Premixed 41 Plex (catalog no. HCYTMAG-60K-PX41), MILLIPLEX MAP TGFβ Magnetic Bead 3 Plex Kit (catalog no. TGFBMAG-64K-03), and a custom MILLIPLEX MAP Human T_H17 Panel (catalog no. HTH17MAG-14K-10). The protein standards were reconstituted in CM, and we serially diluted the protein stock to generate an eight-point standard curve. Samples were analyzed with the Bio-Plex 3D Suspension Array System (Bio-Rad Laboratories Inc.). Data were collected using the xPONENT for FLEXMAP 3D software, version 4.2 (Luminex Corporation, Austin, TX, USA). Concentration of each analyte was determined from a standard curve, which was generated by fitting a five-parameter logistic regression of mean fluorescence on known concentrations of each analyte (Bio-Plex Manager software). To concurrently evaluate all cytokine/chemokine concentration values and identify multi-analyte profiles, samples were assessed using PCA, an unsupervised dimensionality reduction technique. PCA was implemented using MATLAB (version 2018b, MathWorks). To evaluate the effect of SCFA treatment, samples were collapsed into log_2 fold-change values. Specifically, fold-change ratios were calculated using the mean of samples treated with SCFA from a given disease background, T cell experimental setup, and media compartment and the mean of samples without SCFA treatment from the same experimental setup. The statistical significance of log_2 fold-change values was determined from a two-sample t test using all biological replicates for each of the two groups in the comparison. Values were corrected for multiple hypothesis testing using the Benjamini–Hochberg method. Values were calculated using MATLAB and visualized using Prism

(Version-8.3.0, GraphPad Software). Hierarchical complete clustering, heatmaps, and PCA of cytokine concentrations were performed using ClustVis, an online platform integrating several R packages for analysis. Cytokine data were normalized by mean-centering and variance scaling before clustering and PCA. Actual cytokine/chemokine and neuronal marker concentrations were plotted in Prism 8.0 (GraphPad Software). Paired t test was used to calculate statistical significance.

Metabolomics

Broad discovery metabolomic analysis and bioinformatic data processing were performed by Metabolon (Metabolon Inc., Durham, NC, USA). Samples from the cerebral MPSs in isolation were subject to metabolite extractions and analysis by reversed-phase ultra-performance liquid chromatography–tandem mass spectrometry (RP/UPLC-MS/MS) (ESI+) (−ESI) with details of the methods published previously (78). Following receipt, samples were inventoried and immediately stored at −80°C. Each sample received was accessioned into the Metabolon Laboratory Information Management System (LIMS) and assigned by the LIMS, a unique identifier that was associated with the original source identifier only. This identifier was used to track all sample handling, tasks, results, etc. The samples (and all derived aliquots) were tracked by the LIMS. All portions of any sample were automatically assigned their own unique identifiers by the LIMS when a new task was created; the relationship of these samples was also tracked. All samples were maintained at −80°C until processing.

Global metabolomic discovery

We have performed the global metabolomic discovery on control CM and media collected from the apical and basal compartment of cerebral MPSs in isolation. As per previously established protocols (8), samples were prepared using the automated MicroLab STAR system from Hamilton Company. Several recovery standards were added before the first step in the extraction process for quality control (QC) purposes. To remove protein, small molecules bound to protein or trapped in the precipitated protein matrix were dissociated, and to recover chemically diverse metabolites, proteins were precipitated with methanol under vigorous shaking for 2 min (Glen Mills GenoGrinder 2000) followed by centrifugation. The resulting extract was divided into five fractions: two for analysis by two separate RP/UPLC-MS/MS methods with positive-ion mode electrospray ionization (ESI), one for analysis by RP/UPLC-MS/MS with negative-ion mode ESI, one for analysis by HILIC/UPLC-MS/MS with negative-ion mode ESI, and one sample was reserved for backup. Samples were placed briefly on a TurboVap (Zymark) to remove the organic solvent. The sample extracts were stored overnight under nitrogen before preparation for analysis.

Several types of controls were analyzed in concert with the experimental samples: A pooled matrix sample generated by taking a small volume of each experimental sample (or, alternatively, use of a pool of well-characterized human plasma) served as a technical replicate throughout the dataset; extracted water samples served as process blanks; and a cocktail of QC standards that were carefully chosen not to interfere with the measurement of endogenous compounds were spiked into every analyzed sample, allowing instrument performance monitoring and aiding chromatographic alignment. Instrument variability was determined by calculating the median relative standard deviation (RSD) for the standards that were added to each sample before injection into the mass spectrometers. Overall

process variability was determined by calculating the median RSD for all endogenous metabolites (i.e., noninstrument standards) present in 100% of the pooled matrix samples. Experimental samples were randomized across the platform run with QC samples spaced evenly among the injections.

All methods used a Waters ACQUITY UPLC and a Thermo Fisher Scientific Q-Exactive high resolution/accurate mass spectrometer interfaced with a heated ESI (HESI-II) source and Orbitrap mass analyzer operated at 35,000 mass resolution. The sample extract was dried and then reconstituted in solvents compatible with each of the four methods. Each reconstitution solvent contained a series of standards at fixed concentrations to ensure injection and chromatographic consistency. One aliquot was analyzed using acidic positive-ion conditions, chromatographically optimized for more hydrophilic compounds. In this method, the extract was gradient eluted from a C18 column (Waters UPLC BEH C18; 2.1 × 100 mm, 1.7 μm) using water and methanol, containing 0.05% perfluoropentanoic acid (PFPA) and 0.1% formic acid (FA). Another aliquot was also analyzed using acidic positive-ion conditions; however, it was chromatographically optimized for more hydrophobic compounds. In this method, the extract was gradient eluted from the same aforementioned C18 column using methanol, acetonitrile, water, 0.05% PFPA, and 0.01% FA and was operated at an overall higher organic content. Another aliquot was analyzed using basic negative ion–optimized conditions using a separate dedicated C18 column. The basic extracts were gradient-eluted from the column using methanol and water, but with 6.5 mM ammonium bicarbonate at pH 8. The fourth aliquot was analyzed via negative ionization following elution from a HILIC column (Waters UPLC BEH Amide; 2.1 × 150 mm, 1.7 μm) using a gradient consisting of water and acetonitrile with 10 mM ammonium formate (pH 10.8). The MS analysis alternated between MS and data-dependent MSn scans using dynamic exclusion. The scan range varied slightly between methods but covered 70 to 1000 mass/charge ratio (m/z). Raw data files are archived.

Bioinformatic analysis of identified targets

The Metabolon informatics system consisted of four major components, the LIMS, the data extraction and peak-identification software, data processing tools for QC and compound identification, and a collection of information interpretation and visualization tools for use by data analysts. The hardware and software foundations for these informatics components were the LAN backbone and a database server running Oracle 10.2.0.1 Enterprise Edition (8).

Raw data were extracted, peak-identified, and QC-processed using Metabolon's hardware and software. These systems are built on a web-service platform using Microsoft's .NET technologies, which run on high-performance application servers and fiber-channel storage arrays in clusters to provide active failover and load-balancing. Compounds were identified by comparison to library entries of purified standards or recurrent unknown entities. Metabolon maintains a library based on authenticated standards that contains the retention time/index (RI), m/z, and chromatographic data (including MS/MS spectral data) on all molecules present in the library. Furthermore, biochemical identifications are based on three criteria: retention index within a narrow RI window of the proposed identification, accurate mass match to the library ±10 ppm, and the MS/MS forward and reverse scores between the experimental data and authentic standards. The MS/MS scores are based on a comparison of the ions present in the experimental spectrum to the ions present in the library spectrum. While there may be similarities between these

molecules based on one of these factors, the use of all three data points can be used to distinguish and differentiate biochemicals. More than 3300 commercially available purified standard compounds have been acquired and registered into LIMS for analysis on all platforms for determination of their analytical characteristics. Additional mass spectral entries have been created for structurally unnamed biochemicals that have been identified by virtue of their recurrent nature (both chromatographic and mass spectral). These compounds have the potential to be identified by future acquisition of a matching purified standard or by classical structural analysis.

Peaks were quantified using area under the curve. For samples analyzed on different days, a data normalization step was performed to correct variation resulting from instrument inter-day tuning differences. Essentially, each compound was corrected in run-day blocks by registering the medians to equal one (1.00) and normalizing each data point proportionately (termed the "block correction"). For studies that did not require more than 1 day of analysis, no normalization is necessary, other than for purposes of data visualization. In certain instances, biochemical data may have been normalized to an additional factor (e.g., cell counts, total protein as determined by Bradford assay, osmolality, etc.) to account for differences in metabolite levels due to differences in the amount of material present in each sample. Two types of statistical analysis are usually performed: (i) significance tests and (ii) classification analysis. Standard statistical analyses are performed in ArrayStudio on log-transformed data. For those analyses not standard in ArrayStudio, the programs R (http://cran.r-project.org/) or JMP were used. Pathway enrichment analysis and visualization were performed with Metabolons proprietary Pathway Explorer tool.

RNA-seq

Library preparation, sequencing, and analysis were performed by the BioMicro Center at MIT.

RNA extraction, cDNA library preparation, and next-generation sequencing

Neurons, astrocytes, and microglia from the cerebral MPSs were jointly collected, and mRNA was extracted using the PureLink RNA mini kit (Thermo Fisher Scientific, catalog no. 12183018A). Total RNA was analyzed and quantified using the Fragment Analyzer (Advanced Analytical). RNA sequencing (RNA-seq) libraries were prepared using a volume reduced version of the New England Biolabs ribosomal reduction chemistry and RNA-seq library construction kit (Mildrum et al., in preparation). In brief, RNA quality and quantity were confirmed using an Agilent Fragment Analyzer and ribosomal RNA (rRNA) was depleted from 50 ng of total RNA using the NEBNext Ribodepletion kit (New England Biolabs) at a 1:6 ratio from the standard protocol using a Mosquito HV automated liquid handler (TTP Labtech). The resulting depleted RNA is then fragmented and converted to cDNA, and indexed Illumina libraries are constructed using the NEBNext Ultra II Directional RNA Library Construction Kit (New England Biolabs) at a 1:10 ratio from the standard protocol using the Mosquito HV. Final libraries are quantified using SYBRgreen on a Varioskan plate reader and spot-checked using the Agilent Fragment Analyzer. Samples were pooled and quantified by quantitative polymerase chain reaction before Illumina sequencing on a HiSeq2000 using 40-nt single-end reads.

RNA-seq data analysis

Quality control: Reads were aligned against the hg19 (Feb 2009) human genome assembly using bwa mem v. 0.7.12-r1039

[http://bio-bwa.sourceforge.net/] with flags –t 16 –f and mapping rates, fraction of multiply-mapping reads, number of unique 20-mers at the 5′ end of the reads, and insert size distributions; fraction of rRNAs were calculated using bedtools v. 2.25.0. In addition, each resulting bam file was randomly down-sampled to a million reads, which were aligned against hg19, and read density across genomic features was estimated for RNA-seq–specific quality control metrics. RNA-seq mapping and quantitation: Reads were aligned against GRCh38/ENSEMBL 89 annotation using STAR v. 2.5.3a with the following flags: -runThreadN 8 --runMode alignReads --outFilterType BySJout --outFilterMultimapNmax 20 --alignSJoverhangMin 8 --alignSJDBoverhangMin 1 --outFilterMismatchNmax 999 --alignIntronMin 10 --alignIntronMax 1000000 --alignMatesGapMax 1000000 --outSAMtype BAM SortedByCoordinate --quantMode TranscriptomeSAM with --genomeDir pointing to a 75-nt junction GRCh38 STAR suffix array. Gene expression was quantitated using RSEM v. 1.3.0 with the following flags for all libraries: rsem-calculate-expression --calc-pme --alignments -p 8 --forward-prob 0 against an annotation matching the STAR SA reference. Posterior mean estimates (pme) of counts and estimated RPKM were retrieved.

DGE analysis

To identify significantly altered genes in isolation versus interaction conditions, differential gene analysis of count data was performed using DESeq2 (Version 1.12.3) in R as described previously (8). Dataset parameters were estimated using the estimateSizeFactors() and estimateDispersions() functions; read counts across conditions were modeled on the basis of a negative binomial distribution and a Wald test was used to test for differential expression [nbinomWaldtest(), all packaged into the DESeq() function], using the treatment type as a contrast. Fold changes, P values, and Benjamin-Hochberg–adjusted P values (BH) were reported for each protein-coding gene. Regularized fold changes were calculated using the lfcShrink() function.

GSEA, pathway enrichment, gene ontology analysis, and visualization

Differential expression results from DESeq2 were retrieved, and the "stat" column was used to prerank genes for gene set enrichment analysis (GSEA) analysis. Briefly, the stat values reflect the Wald's test performed on read counts as modeled by DESeq2 using the negative binomial distribution. Genes that were not expressed were excluded from the analysis. GSEA (version 2.2.3) was performed to identify differentially regulated gene sets in isolation versus interaction, as described previously (79). To stabilize variance, the normalized count data were processed using a regularized logarithm transformation in DESeq2. The signal-to-noise metric was used to generate the ranked list of genes. The empirical P values for each enrichment score were calculated relative to the null distribution of enrichment scores, which was computed via 1000 gene set permutations. Gene sets with nominal P < 0.05 and q value < 0.05 were considered significant. Volcano plots of differentially expressed genes were made with plot.ly (Plotly). Positive or negative fold changes of DGEs were analyzed separately for enrichments. Pathway analysis and gene ontology term analysis based on various databases were performed using the following tools: OmicsNet, Enrichr, g:Profiler, and ClueGO in Cytoscape. ClueGO was also used for visualization of significantly enriched WikiPathways networks where size and color intensity of nods correspond to significance of enrichments.

SUPPLEMENTARY MATERIALS

Supplementary material for this article is available at http://advances.sciencemag.org/cgi/content/full/7/5/eabd1707/DC1

View/request a protocol for this paper from *Bio-protocol*.

REFERENCES AND NOTES

1. T. R. Sampson, J. W. Debelius, T. Thron, S. Janssen, G. G. Shastri, Z. E. Ilhan, C. Challis, C. E. Schretter, S. Rocha, V. Gradinaru, M.-F. Chesselet, A. Keshavarzian, K. M. Shannon, R. Krajmalnik-Brown, P. Wittung-Stafshede, R. Knight, S. K. Mazmanian, Gut microbiota regulate motor deficits and neuroinflammation in a model of Parkinson's disease. *Cell* **167**, 1469–1480.e12 (2016).

2. C. R. Martin, V. Osadchiy, A. Kalani, E. A. Mayer, The brain-gut-microbiome axis. *Cell. Mol. Gastroenterol. Hepatol.* **6**, 133–148 (2018).

3. B. Dalile, L. Van Oudenhove, B. Vervliet, K. Verbeke, The role of short-chain fatty acids in microbiota-gut-brain communication. *Nat. Rev. Gastroenterol. Hepatol.* **16**, 461–478 (2019).

4. F. Soldner, Y. Stelzer, C. S. Shivalila, B. J. Abraham, J. C. Latourelle, M. I. Barrasa, J. Goldmann, R. H. Myers, R. A. Young, R. Jaenisch, Parkinson-associated risk variant in distal enhancer of α-synuclein modulates target gene expression. *Nature* **533**, 95–99 (2016).

5. F. Soldner, J. Laganière, A. W. Cheng, D. Hockemeyer, Q. Gao, R. Alagappan, V. Khurana, L. I. Golbe, R. H. Myers, S. Lindquist, L. Zhang, D. Guschin, L. K. Fong, B. J. Vu, X. Meng, F. D. Urnov, E. J. Rebar, P. D. Gregory, H. S. Zhang, R. Jaenisch, Generation of isogenic pluripotent stem cells differing exclusively at two early onset Parkinson point mutations. *Cell* **146**, 318–331 (2011).

6. A. Burberry, M. F. Wells, F. Limone, A. Couto, K. S. Smith, J. Keaney, G. Gillet, N. van Gastel, J. Y. Wang, O. Pietilainen, M. Qian, P. Eggan, C. Cantrell, J. Mok, I. Kadiu, D. T. Scadden, K. Eggan, *C9orf72* suppresses systemic and neural inflammation induced by gut bacteria. *Nature* **582**, 89–94 (2020).

7. A. Koh, F. De Vadder, P. Kovatcheva-Datchary, F. Backhed, From dietary fiber to host physiology: Short-chain fatty acids as key bacterial metabolites. *Cell* **165**, 1332–1345 (2016).

8. M. Trapecar, C. Communal, J. Velazquez, C. A. Maass, Y.-J. Huang, K. Schneider, C. W. Wright, V. Butty, G. Eng, O. Yilmaz, D. Trumper, L. G. Griffith, Gut-liver physiomimetics reveal paradoxical modulation of IBD-related inflammation by short-chain fatty acids. *Cell Syst.* **10**, 223–239.e9 (2020).

9. K. Ronaldson-Bouchard, G. Vunjak-Novakovic, Organs-on-a-Chip: A fast track for engineered human tissues in drug development. *Cell Stem Cell* **22**, 310–324 (2018).

10. Y. Tang, Y. Chen, H. Jiang, D. Nie, Short-chain fatty acids induced autophagy serves as an adaptive strategy for retarding mitochondria-mediated apoptotic cell death. *Cell Death Differ.* **18**, 602–618 (2011).

11. G. Noel, N. W. Baetz, J. F. Staab, M. Donowitz, O. Kovbasnjuk, M. F. Pasetti, N. C. Zachos, A primary human macrophage-enteroid co-culture model to investigate mucosal gut physiology and host-pathogen interactions. *Sci. Rep.* **7**, 45270 (2017).

12. T. J. Long, P. A. Cosgrove, R. T. Dunn II, D. B. Stolz, H. Hamadeh, C. Afshari, H. McBride, L. G. Griffith, Modeling therapeutic antibody-small molecule drug-drug interactions using a three-dimensional perfusable human liver coculture platform. *Drug Metab. Dispos.* **44**, 1940–1948 (2016).

13. U. Sarkar, D. Rivera-Burgos, E. M. Large, D. J. Hughes, K. C. Ravindra, R. L. Dyer, M. R. Ebrahimkhani, J. S. Wishnok, L. G. Griffith, S. R. Tannenbaum, Metabolite profiling and pharmacokinetic evaluation of hydrocortisone in a perfused three-dimensional human liver bioreactor. *Drug Metab. Dispos.* **43**, 1091–1099 (2015).

14. A. M. Clark, S. E. Wheeler, C. L. Young, L. Stockdale, J. Shepard Neiman, W. Zhao, D. B. Stolz, R. Venkataramanan, D. Lauffenburger, L. Griffith, A. Wells, A liver microphysiological system of tumor cell dormancy and inflammatory responsiveness is affected by scaffold properties. *Lab Chip* **17**, 156–168 (2016).

15. X. Li, S. M. George, L. Vernetti, A. H. Gough, D. L. Taylor, A glass-based, continuously zonated and vascularized human liver acinus microphysiological system (vLAMPS) designed for experimental modeling of diseases and ADME/TOX. *Lab Chip* **18**, 2614–2631 (2018).

16. J. Muffat, Y. Li, B. Yuan, M. Mitalipova, A. Omer, S. Corcoran, G. Bakiasi, L. H. Tsai, P. Aubourg, R. M. Ransohoff, R. Jaenisch, Efficient derivation of microglia-like cells from human pluripotent stem cells. *Nat. Med.* **22**, 1358–1367 (2016).

17. D. Sulzer, D. J. Surmeier, Neuronal vulnerability, pathogenesis, and Parkinson's disease. *Mov. Disord.* **28**, 715–724 (2013).

18. K. Atarashi, N. Manel, E. L. Brodie, T. Shima, U. Karaoz, D. Wei, K. C. Goldfarb, C. A. Santee, S. V. Lynch, T. Tanoue, A. Imaoka, K. Itoh, K. Takeda, Y. Umesaki, K. Honda, D. R. Littman, Induction of intestinal Th17 cells by segmented filamentous bacteria. *Cell* **139**, 485–498 (2009).

19. Z. Liu, Y. Huang, B. B. Cao, Y. H. Qiu, Y. P. Peng, Th17 cells induce dopaminergic neuronal death via LFA-1/ICAM-1 interaction in a mouse model of Parkinson's disease. *Mol. Neurobiol.* **54**, 7762–7776 (2017).

20. F. Yang, B. Li, L. Li, H. Zhang, The clinical significance of the imbalance of Th17 and Treg cells and their related cytokines in peripheral blood of Parkinson's disease patients. *Int. J. Clin. Exp. Med.* **9**, 17946–17951 (2016).

21. Z. He, Q. Yu, Identification and characterization of functional modules reflecting transcriptome transition during human neuron maturation. *BMC Genomics* **19**, 262 (2018).

22. J. M. Redwine, C. F. Evans, Markers of central nervous system glia and neurons in vivo during normal and pathological conditions. *Curr. Top. Microbiol. Immunol.* **265**, 119–140 (2002).

23. J. D. Cahoy, B. Emery, A. Kaushal, L. C. Foo, J. L. Zamanian, K. S. Christopherson, Y. Xing, J. L. Lubischer, P. A. Krieg, S. A. Krupenko, W. J. Thompson, B. A. Barres, A transcriptome database for astrocytes, neurons, and oligodendrocytes: A new resource for understanding brain development and function. *J. Neurosci.* **28**, 264–278 (2008).

24. P. Hasel, O. Dando, Z. Jiwaji, P. Baxter, A. C. Todd, S. Heron, N. M. Márkus, J. McQueen, D. W. Hampton, M. Torvell, S. S. Tiwari, S. McKay, A. Eraso-Pichot, A. Zorzano, R. Masgrau, E. Galea, S. Chandran, D. J. A. Wyllie, T. I. Simpson, G. E. Hardingham, Correction: Author correction: Neurons and neuronal activity control gene expression in astrocytes to regulate their development and metabolism. *Nat. Commun.* **9**, 16176 (2018).

25. A. T. McKenzie, M. Wang, M. E. Hauberg, J. F. Fullard, A. Kozlenkov, A. Keenan, Y. L. Hurd, S. Dracheva, P. Casaccia, P. Roussos, B. Zhang, Brain cell type specific gene expression and co-expression network architectures. *Sci. Rep.* **8**, 8868 (2018).

26. R. Timmerman, S. M. Burm, J. J. Bajramovic, An overview of in vitro methods to study microglia. *Front. Cell. Neurosci.* **12**, 242 (2018).

27. M. Cheah, M. R. Andrews, Integrin activation: Implications for axon regeneration. *Cell* **7**, 20 (2018).

28. P. J. Voulalas, L. Holtzclaw, J. Wolstenholme, J. T. Russell, S. E. Hyman, Metabotropic glutamate receptors and dopamine receptors cooperate to enhance extracellular signal-regulated kinase phosphorylation in striatal neurons. *J. Neurosci.* **25**, 3763–3773 (2005).

29. J. E. Vance, Dysregulation of cholesterol balance in the brain: Contribution to neurodegenerative diseases. *Dis. Model. Mech.* **5**, 746–755 (2012).

30. B. A. Plog, M. Nedergaard, The glymphatic system in central nervous system health and disease: Past, present, and future. *Annu. Rev. Pathol.* **13**, 379–394 (2018).

31. M. Addison, Q. Xu, J. Cayuso, D. G. Wilkinson, Cell identity switching regulated by retinoic acid signaling maintains homogeneous segments in the hindbrain. *Dev. Cell* **45**, 606–620.e3 (2018).

32. E. B. Moloney, A. Moskites, E. J. Ferrari, O. Isacson, P. J. Hallett, The glycoprotein GPNMB is selectively elevated in the substantia nigra of Parkinson's disease patients and increases after lysosomal stress. *Neurobiol. Dis.* **120**, 1–11 (2018).

33. K. Tanaka, T. Suzuki, N. Hattori, Y. Mizuno, Ubiquitin, proteasome and parkin. *Biochim. Biophys. Acta* **1695**, 235–247 (2004).

34. E. Janda, L. Boi, A. R. Carta, Microglial phagocytosis and its regulation: A therapeutic target in Parkinson's disease? *Front. Mol. Neurosci.* **11**, 144 (2018).

35. Y. Shinbo, T. Niki, T. Taira, H. Ooe, K. Takahashi-Niki, C. Maita, C. Seino, S. M. M. Iguchi-Ariga, H. Ariga, Proper SUMO-1 conjugation is essential to DJ-1 to exert its full activities. *Cell Death Differ.* **13**, 96–108 (2006).

36. B. Mollenhauer, J. J. Locascio, W. Schulz-Schaeffer, F. Sixel-Döring, C. Trenkwalder, M. G. Schlossmacher, α-Synuclein and tau concentrations in cerebrospinal fluid of patients presenting with parkinsonism: A cohort study. *Lancet Neurol.* **10**, 230–240 (2011).

37. C. Soto, S. Pritzkow, Protein misfolding, aggregation, and conformational strains in neurodegenerative diseases. *Nat. Neurosci.* **21**, 1332–1340 (2018).

38. J. H. Cummings, E. W. Pomare, W. J. Branch, C. P. Naylor, G. T. Macfarlane, Short chain fatty acids in human large intestine, portal, hepatic and venous blood. *Gut* **28**, 1221–1227 (1987).

39. J. Park, M. Kim, S. G. Kang, A. H. Jannasch, B. Cooper, J. Patterson, C. H. Kim, Short-chain fatty acids induce both effector and regulatory T cells by suppression of histone deacetylases and regulation of the mTOR-S6K pathway. *Mucosal Immunol.* **8**, 80–93 (2015).

40. E. Junn, R. D. Ronchetti, M. M. Quezado, S. Y. Kim, M. M. Mouradian, Tissue transglutaminase-induced aggregation of alpha-synuclein: Implications for Lewy body formation in Parkinson's disease and dementia with Lewy bodies. *Proc. Natl. Acad. Sci. U.S.A.* **100**, 2047–2052 (2003).

41. H. Osaka, Y. L. Wang, K. Takada, S. Takizawa, R. Setsuie, H. Li, Y. Sato, K. Nishikawa, Y. J. Sun, M. Sakurai, T. Harada, Y. Hara, I. Kimura, S. Chiba, K. Namikawa, H. Kiyama, M. Noda, S. Aoki, K. Wada, Ubiquitin carboxy-terminal hydrolase L1 binds to and stabilizes monoubiquitin in neuron. *Hum. Mol. Genet.* **12**, 1945–1958 (2003).

42. G. M. Miller, The emerging role of trace amine-associated receptor 1 in the functional regulation of monoamine transporters and dopaminergic activity. *J. Neurochem.* **116**, 164–176 (2011).

43. T. Yamashima, A putative link of PUFA, GPR40 and adult-born hippocampal neurons for memory. *Prog. Neurobiol.* **84**, 105–115 (2008).

44. P. Garcia-Esparcia, K. Hernández-Ortega, A. Koneti, L. Gil, R. Delgado-Morales, E. Castaño, M. Carmona, I. Ferrer, Altered machinery of protein synthesis is region- and stage-dependent and is associated with α-synuclein oligomers in Parkinson's disease. *Acta Neuropathol. Commun.* **3**, 76 (2015).

45. J. P. Bennett Jr., P. M. Keeney, D. G. Brohawn, RNA sequencing reveals small and variable contributions of infectious agents to transcriptomes of postmortem nervous tissues from amyotrophic lateral sclerosis, Alzheimer's disease and Parkinson's disease subjects, and increased expression of genes from disease-activated microglia. *Front. Neurosci.* **13**, 235 (2019).

46. H. Keren-Shaul, A. Spinrad, A. Weiner, O. Matcovitch-Natan, R. Dvir-Szternfeld, T. K. Ulland, E. David, K. Baruch, D. Lara-Astaiso, B. Toth, S. Itzkovitz, M. Colonna, M. Schwartz, I. Amit, A unique microglia type associated with restricting development of Alzheimer's disease. *Cell* **169**, 1276–1290.e17 (2017).

47. D. J. Morrison, T. Preston, Formation of short chain fatty acids by the gut microbiota and their impact on human metabolism. *Gut Microbes* **7**, 189–200 (2016).

48. H. Hochstrasser, P. Bauer, U. Walter, S. Behnke, J. Spiegel, I. Csoti, B. Zeiler, A. Bornemann, J. Pahnke, G. Becker, O. Riess, D. Berg, Ceruloplasmin gene variations and substantia nigra hyperechogenicity in Parkinson's disease. *Neurology* **63**, 1912–1917 (2004).

49. N. Ostrerova-Golts, L. Petrucelli, J. Hardy, J. M. Lee, M. Farer, B. Wolozin, The A53T α-synuclein mutation increases iron-dependent aggregation and toxicity. *J. Neurosci.* **20**, 6048–6054 (2000).

50. N. Golts, H. Snyder, M. Frasier, C. Theisler, P. Choi, B. Wolozin, Magnesium inhibits spontaneous and iron-induced aggregation of α-synuclein. *J. Biol. Chem.* **277**, 16116–16123 (2002).

51. N. Tsamandouras, W. L. K. Chen, C. D. Edington, C. L. Stokes, L. G. Griffith, M. Cirit, Integrated gut and liver microphysiological systems for quantitative in vitro pharmacokinetic studies. *AAPS J.* **19**, 1499–1512 (2017).

52. C. D. Edington, W. L. K. Chen, E. Geishecker, T. Kassis, L. R. Soenksen, B. M. Bhushan, D. Freake, J. Kirschner, C. Maass, N. Tsamandouras, J. Valdez, C. D. Cook, T. Parent, S. Snyder, J. Yu, E. Suter, M. Shockley, J. Velazquez, J. J. Velazquez, L. Stockdale, J. P. Papps, I. Lee, N. Vann, M. Gamboa, M. E. LaBarge, Z. Zhong, X. Wang, L. A. Boyer, D. A. Lauffenburger, R. L. Carrier, C. Communal, S. R. Tannenbaum, C. L. Stokes, D. J. Hughes, G. Rohatgi, D. L. Trumper, M. Cirit, L. G. Griffith, Interconnected microphysiological systems for quantitative biology and pharmacology studies. *Sci. Rep.* **8**, 4530 (2018).

53. L. Vernetti, A. Gough, N. Baetz, S. Blutt, J. R. Broughman, J. A. Brown, J. Foulke-Abel, N. Hasan, J. In, E. Kelly, O. Kovbasnjuk, J. Repper, N. Senutovitch, J. Stabb, C. Yeung, N. C. Zachos, M. Donowitz, M. Estes, J. Himmelfarb, G. Truskey, J. P. Wikswo, D. L. Taylor, Functional coupling of human microphysiology systems: Intestine, liver, kidney proximal tubule, blood-brain barrier and skeletal muscle. *Sci. Rep.* **7**, 42296 (2017).

54. B. M. Maoz, A. Herland, E. A. FitzGerald, T. Grevesse, C. Vidoudez, A. R. Pacheco, S. P. Sheehy, T. E. Park, S. Dauth, R. Mannix, N. Budnik, K. Shores, A. Cho, J. C. Nawroth, B. Segrè, B. Budnik, D. E. Ingber, K. K. Parker, A linked organ-on-chip model of the human neurovascular unit reveals the metabolic coupling of endothelial and neuronal cells. *Nat. Biotechnol.* **36**, 865–874 (2018).

55. C. W. McAleer, C. J. Long, D. Elbrecht, T. Sasserath, L. R. Bridges, J. W. Rumsey, C. Martin, M. Schnepper, Y. Wang, F. Schuler, A. B. Roth, C. Funk, M. L. Shuler, J. J. Hickman, Multi-organ system for the evaluation of efficacy and off-target toxicity of anticancer therapeutics. *Sci. Transl. Med.* **11**, eaav1386 (2019).

56. S. Bauer, C. Wennberg Huldt, K. P. Kanebratt, I. Durieux, D. Gunne, S. Andersson, L. Ewart, W. G. Haynes, I. Maschmeyer, A. Winter, C. Ämmälä, U. Marx, T. B. Andersson, Functional coupling of human pancreatic islets and liver spheroids on-a-chip: Towards a novel human ex vivo type 2 diabetes model. *Sci. Rep.* **7**, 14620 (2017).

57. V. Hernandez-Gordillo, T. Kassis, A. Lampejo, G. H. Choi, M. E. Gamboa, J. S. Gnecco, A. Brown, D. T. Breault, R. Carrier, L. G. Griffith, Fully synthetic matrices for in vitro culture of primary human intestinal enteroids and endometrial organoids. *Biomaterials* **254**, 120125 (2020).

58. Y. Wang, R. Kim, D. B. Gunasekara, M. I. Reed, M. DiSalvo, D. L. Nguyen, S. J. Bultman, C. E. Sims, S. T. Magness, N. L. Allbritton, Formation of human colonic crypt array by application of chemical gradients across a shaped epithelial monolayer. *Cell. Mol. Gastroenterol. Hepatol.* **5**, 113–130 (2018).

59. A. Wells, H. S. Wiley, A systems perspective of heterocellular signaling. *Essays Biochem.* **62**, 607–617 (2018).

60. G. L. Medlock, T. J. Moutinho, J. A. Papin, Medusa: Software to build and analyze ensembles of genome-scale metabolic network reconstructions. *PLoS Comput. Biol.* **16**, e1007847 (2020).

61. A. R. Soltis, S. Motola, S. Vernia, C. W. Ng, N. J. Kennedy, S. Dalin, B. J. Matthews, R. J. Davis, E. Fraenkel, Hyper- and hypo- nutrition studies of the hepatic transcriptome and epigenome suggest that PPARα regulates anaerobic glycolysis. *Sci. Rep.* **7**, 174 (2017).

62. M. M. Unger, J. Spiegel, K. U. Dillmann, D. Grundmann, H. Philippeit, J. Bürmann, K. Faßbender, A. Schwiertz, K. H. Schäfer, Short chain fatty acids and gut microbiota differ between patients with Parkinson's disease and age-matched controls. *Parkinsonism Relat. Disord.* **32**, 66–72 (2016).

63. Y. Furusawa, Y. Obata, S. Fukuda, T. A. Endo, G. Nakato, D. Takahashi, Y. Nakanishi, C. Uetake, K. Kato, T. Kato, M. Takahashi, N. N. Fukuda, S. Murakami, E. Miyauchi, S. Hino, K. Atarashi, S. Onawa, Y. Fujimura, T. Lockett, J. M. Clarke, D. L. Topping, M. Tomita, S. Hori, O. Ohara, T. Morita, H. Koseki, J. Kikuchi, K. Honda, K. Hase, H. Ohno, Commensal microbe-derived butyrate induces the differentiation of colonic regulatory T cells. *Nature* **504**, 446–450 (2013).

64. M. Luu, K. Weigand, F. Wedi, C. Breidenbend, H. Leister, S. Pautz, T. Adhikary, A. Visekruna, Regulation of the effector function of CD8$^+$ T cells by gut microbiota-derived metabolite butyrate. *Sci. Rep.* **8**, 14430 (2018).

65. J. L. Goldstein, M. S. Brown, Regulation of the mevalonate pathway. *Nature* **343**, 425–430 (1990).

66. S. S. S. Saravi, S. S. S. Saravi, K. Khoshbin, A. R. Dehpour, Current insights into pathogenesis of Parkinson's disease: Approach to mevalonate pathway and protective role of statins. *Biomed. Pharmacother.* **90**, 724–730 (2017).

67. S. Fanning, A. Haque, T. Imberdis, V. Baru, M. I. Barrasa, S. Nuber, D. Termine, N. Ramalingam, G. P. H. Ho, T. Noble, J. Sandoe, Y. Lou, D. Landgraf, Y. Freyzon, G. Newby, F. Soldner, E. Terry-Kantor, T.-E. Kim, H. F. Hofbauer, M. Becuwe, R. Jaenisch, D. Pincus, C. B. Clish, T. C. Walther, R. V. Farese Jr., S. Srinivasan, M. A. Welte, S. D. Kohlwein, U. Dettmer, S. Lindquist, D. Selkoe, Lipidomic analysis of α-synuclein neurotoxicity identifies stearoyl CoA desaturase as a target for Parkinson treatment. *Mol. Cell* **73**, 1001–1014.e8 (2019).

68. R. F. Keep, H. C. Jones, L. R. Drewes, The year in review: Progress in brain barriers and brain fluid research in 2018. *Fluids Barriers CNS* **16**, 4 (2019).

69. H. Uwamori, Y. Ono, T. Yamashita, K. Arai, R. Sudo, Comparison of organ-specific endothelial cells in terms of microvascular formation and endothelial barrier functions. *Microvasc. Res.* **122**, 60–70 (2019).

70. J. G. DeStefano, J. J. Jamieson, R. M. Linville, P. C. Searson, Benchmarking in vitro tissue-engineered blood-brain barrier models. *Fluids Barriers CNS* **15**, 32 (2018).

71. S. Shetty, P. F. Lalor, D. H. Adams, Liver sinusoidal endothelial cells - gatekeepers of hepatic immunity. *Nat. Rev. Gastroenterol. Hepatol.* **15**, 555–567 (2018).

72. S. J. Dixon, K. M. Lemberg, M. R. Lamprecht, R. Skouta, E. M. Zaitsev, C. E. Gleason, D. N. Patel, A. J. Bauer, A. M. Cantley, W. S. Yang, B. Morrison III, B. R. Stockwell, Ferroptosis: An iron-dependent form of nonapoptotic cell death. *Cell* **149**, 1060–1072 (2012).

73. B. R. Stockwell, J. P. Friedmann Angeli, H. Bayir, A. I. Bush, M. Conrad, S. J. Dixon, S. Fulda, S. Gascón, S. K. Hatzios, V. E. Kagan, K. Noel, X. Jiang, A. Linkermann, M. E. Murphy, M. Overholtzer, A. Oyagi, G. C. Pagnussat, J. Park, Q. Ran, C. S. Rosenfeld, K. Salnikow, D. Tang, F. M. Torti, S. V. Torti, S. Toyokuni, K. A. Woerpel, D. D. Zhang, Ferroptosis: A regulated cell death nexus linking metabolism, redox biology, and disease. *Cell* **171**, 273–285 (2017).

74. S. J. Guiney, P. A. Adlard, A. I. Bush, D. I. Finkelstein, S. Ayton, Ferroptosis and cell death mechanisms in Parkinson's disease. *Neurochem. Int.* **104**, 34–48 (2017).

75. J. Roper, T. Tammela, N. M. Cetinbas, A. Akkad, A. Roghanian, S. Rickelt, M. Almeqdadi, K. Wu, M. A. Oberli, F. J. Sánchez-Rivera, Y. K. Park, X. Liang, G. Eng, M. S. Taylor, R. Azimi, D. Kedrin, R. Neupane, S. Beyaz, E. T. Sicinska, Y. Suarez, J. Yoo, L. Chen, L. Zukerberg, P. Katajisto, V. Deshpande, A. J. Bass, P. N. Tsichlis, J. Lees, R. Langer, R. O. Hynes, J. Chen, A. Bhutkar, T. Jacks, Ö. H. Yilmaz, In vivo genome editing and organoid transplantation models of colorectal cancer and metastasis. *Nat. Biotechnol.* **35**, 569–576 (2017).

76. L. I. Golbe, A. M. Lazzarini, R. C. Duvoisin, G. D. Iorio, G. Sanges, V. Bonavita, S. la Sala, Clinical genetic analysis of Parkinson's disease in the Contursi kindred. *Ann. Neurol.* **40**, 767–775 (1996).

77. P. Douvaras, B. Sun, M. Wang, I. Kruglikov, G. Lallos, M. Zimmer, C. Terrenoire, B. Zhang, S. Gandy, E. Schadt, D. O. Freytes, S. Noggle, V. Fossati, Directed differentiation of human pluripotent stem cells to microglia. *Stem Cell Rep.* **8**, 1516–1524 (2017).

78. A. M. Evans, B. R. Bridgewater, Q. Liu, M. W. Mitchell, R. J. Robinson, H. Dai, S. J. Stewart, C. D. DeHaven, L. A. D. Miller, High resolution mass spectrometry improves data quantity and quality as compared to unit mass resolution mass spectrometry in high-throughput profiling metabolomics. *Metabolomics* **4**, 132 (2014).

79. A. Subramanian, P. Tamayo, V. K. Mootha, S. Mukherjee, B. L. Ebert, M. A. Gillette, A. Paulovich, S. L. Pomeroy, T. R. Golub, E. S. Lander, J. P. Mesirov, Gene set enrichment analysis: A knowledge-based approach for interpreting genome-wide expression profiles. *Proc. Natl. Acad. Sci. U.S.A.* **102**, 15545–15550 (2005).

80. C. R. Chapman, C. Reyes, V. Gupta, Normal physiological levels of human cytokines using Bio-Plex Pro™ cytokine assays, Bio-Rad Tech. Note (2010).

81. K. Alnek, K. Kisand, K. Heilman, A. Peet, K. Varik, R. Uibo, Increased blood levels of growth factors, proinflammatory cytokines, and Th17 cytokines in patients with newly diagnosed type 1 diabetes. *PLOS ONE* **10**, e0142976 (2015).

82. L. M. Wakefield, J. J. Letterio, T. Chen, D. Danielpour, R. S. Allison, L. H. Pai, A. M. Denicoff, M. H. Noone, K. H. Cowan, J. A. O'Shaughnessy, Transforming growth factor-beta1 circulates in normal human plasma and is unchanged in advanced metastatic breast cancer. *Clin. Cancer Res.* **1**, 129–136 (1995).

83. I. Agalliu, X. Xue, M. Cushman, E. Cornell, A. W. Hsing, R. C. Kaplan, K. Anastos, S. Rajpathak, G. Y. F. Ho, Detectability and reproducibility of plasma levels of chemokines and soluble receptors. *Results Immunol.* **3**, 79–84 (2013).

84. H. O. Kim, H.-S. Kim, J. C. Youn, E.-C. Shin, S. Park, Serum cytokine profiles in healthy young and elderly population assessed using multiplexed bead-based immunoassays. *J. Transl. Med.* **9**, 113 (2011).

85. G. Kleiner, V. Zanin, L. Monasta, S. Crovella, L. Caruso, D. Milani, A. Marcuzzi, Pediatric patients with inflammatory bowel disease exhibit increased serum levels of proinflammatory cytokines and chemokines, but decreased circulating levels of macrophage inhibitory protein-1β, interleukin-2 and interleukin-17. *Exp. Ther. Med.* **9**, 2047–2052 (2015).

86. G. Kleiner, A. Marcuzzi, V. Zanin, L. Monasta, G. Zauli, Cytokine levels in the serum of healthy subjects. *Mediators Inflamm.* **2013**, 434010 (2013).

87. K. D. Sekiyama, M. Yoshiba, A. W. Thomson, Circulating proinflammatory cytokines (IL-1 β, TNF-α, and IL-6) and IL-1 receptor antagonist (IL-1Ra) in fulminant hepatic failure and acute hepatitis. *Clin. Exp. Immunol.* **98**, 71–77 (1994).

88. M. Shi, J. Bradner, A. M. Hancock, K. A. Chung, J. F. Quinn, E. R. Peskind, D. Galasko, J. Jankovic, C. P. Zabetian, H. M. Kim, J. B. Leverenz, T. J. Montine, C. Ginghina, U. J. Kang, K. C. Cain, Y. Wang, J. Aasly, D. Goldstein, J. Zhang, Cerebrospinal fluid biomarkers for Parkinson disease diagnosis and progression. *Ann. Neurol.* **69**, 570–580 (2011).

89. T. Khaibullin, V. Ivanova, E. Martynova, G. Cherepnev, F. Khabirov, E. Granatov, A. Rizvanov, S. Khaiboullina, Elevated levels of proinflammatory cytokines in cerebrospinal fluid of multiple sclerosis patients. *Front. Immunol.* **8**, 531 (2017).

90. M. P. Vawter, O. Dillon-Carter, W. W. Tourtellotte, P. Carvey, W. J. Freed, TGFβ1 and TGFβ2 concentrations are elevated in Parkinson's disease in ventricular cerebrospinal fluid. *Exp. Neurol.* **142**, 313–322 (1996).

91. D. Westhoff, J. Witlox, L. Koenderman, K. J. Kalisvaart, J. F. M. de Jonghe, M. F. M. van Stijn, A. P. J. Houdijk, I. C. M. Hoogland, A. M. J. Maclullich, D. J. van Westerloo, D. van de Beek, P. Eikelenboom, W. A. van Gool, Preoperative cerebrospinal fluid cytokine levels and the risk of postoperative delirium in elderly hip fracture patients. *J. Neuroinflammation* **10**, 122 (2013).

92. L. Sosvorova, J. Vcelak, M. Mohapl, M. Vitku, M. Bicikova, R. Hampl, Selected pro- and anti-inflammatory cytokines in cerebrospinal fluid in normal pressure hydrocephalus. *Neuro Endocrinol. Lett.* **35**, 586–593 (2014).

93. A. Abdelhak, T. Hottenrott, E. Morenas-Rodríguez, M. Suárez-Calvet, U. K. Zettl, C. Haass, S. G. Meuth, S. Rauer, M. Otto, H. Tumani, A. Huss, Glial activation markers in CSF and serum from patients with primary progressive multiple sclerosis: Potential of serum GFAP as disease severity marker? *Front. Neurol.* **10**, 280 (2019).

94. K. Mokuno, K. Kato, K. Kawai, Y. Matsuoka, T. Yanagi, I. Sobue, Neuron-specific enolase and S-100 protein levels in cerebrospinal fluid of patients with various neurological diseases. *J. Neurol. Sci.* **60**, 443–451 (1983).

Citation: M. Trapecar, E. Wogram, D. Svoboda, C. Communal, A. Omer, T. Lungjangwa, P. Sphabmixay, J. Velazquez, K. Schneider, C. W. Wright, S. Mildrum, A. Hendricks, S. Levine, J. Muffat, M. J. Lee, D. A. Lauffenburger, D. Trumper, R. Jaenisch, L. G. Griffith, Human physiomimetic model integrating microphysiological systems of the gut, liver, and brain for studies of neurodegenerative diseases. *Sci. Adv.* **7**, eabd1707 (2021).

Science Advances

Human physiomimetic model integrating microphysiological systems of the gut, liver, and brain for studies of neurodegenerative diseases

Martin Trapecar, Emile Wogram, Devon Svoboda, Catherine Communal, Attya Omer, Tenzin Lungjangwa, Pierre Sphabmixay, Jason Velazquez, Kirsten Schneider, Charles W. Wright, Samuel Mildrum, Austin Hendricks, Stuart Levine, Julien Muffat, Meelim Jasmine Lee, Douglas A. Lauffenburger, David Trumper, Rudolf Jaenisch, and Linda G. Griffith

View the article online
https://www.science.org/doi/10.1126/sciadv.abd1707
Permissions
https://www.science.org/help/reprints-and-permissions

Use of this article is subject to the Terms of service